# Magneto-Dielectric phenomena in charge and spin frustrated system of layered iron oxide

Makoto Naka, Aya Nagano*, and Sumio Ishihara

*Department of Physics, Tohoku University, Sendai 980-8578, Japan*

(Dated: September 7, 2021)

Dielectric and magnetic phenomena in spin and charge frustrated system $RFe_2O_4$ ($R$ is a rare-earth metal ion) are studied. An electronic model for charge, spin and orbital degrees in a pair of triangular-lattice planes is derived. We analyze this model by utilizing the mean-field approximation and the Monte-Carlo simulation in a finite size cluster. A three fold-type charge ordered structure with charge imbalance between the planes is stabilized in finite temperatures. This polar charge order is reinforced by spin ordering of Fe ions. This novel magneto-dielectric phenomenon is caused by spin frustration and charge-spin coupling in the exchange interaction. We show cross-correlation effect in magnetic- and electric-field responses. Oxygen deficiency effect as an impurity effect in a frustrated charge-spin coupled system is also examined.

## I. INTRODUCTION

Simultaneous existence of electric and magnetic polarizations and their control by external field have been recently revived as multiferroic phenomena in correlated electron oxides.[1,2,3,4] Behind large coupling between electric and magnetic moments, spin frustration plays dominant roles on multiferroic properties. Non-colinear spin structures, such as cycroid, spiral and so on, are realized on a frustrated geometry, and spontaneous electric polarization is induced to gain the symmetric/anti-symmetric exchange interactions.[5,6,7] In this viewpoints, this class of materials are recognized as a spin driven ferroelectricity. Another class of ferroelectricity is possible in correlated electron systems. Apart from the integer filling of electron in valence bands, charge degree of freedom is active. In particular, around the quarter filling, the long-range charge order due to electron correlation is ubiquitously observed in several transition-metal compounds.[8,9,10] When electronic charge is ordered without inversion symmetry, a macroscopic electric polarization appears. This is a ferroelectricity driven by electronic charge degree of freedom. This class of ferroelectricity is realized in low-dimensional organic salts, such as the neutral-ionic transition system[11,12] and $\alpha$-$(BEDT-TTF)_2I_3$.[13] Charge polarized state observed in a layered structure manganite $Pr(Sr_{0.1}Ca_{0.9})_2Mn_2O_7$ is attributed to the charge-orbital order associated with lattice distortion.[14] A possibility of ferroelectricty in manganites is also proposed in theoretical viewpoint.[15]

Rare-earth iron oxides with layered crystal structure $RFe_2O_4$ ($R$=Lu, Y, Yb, Er)[16] of the present interest belong to this class of ferroelectricity. Crystal structure of $RFe_2O_4$ consists of paired Fe-O triangular-lattice layers and $R$-O blocks stacked along the $c$ axis. Schematic view of a paired Fe-O layer, termed the W-layer, is shown in Fig. 1(a). Average valence of Fe ions is +2.5, implying that equal amounts of $Fe^{2+}$ and $Fe^{3+}$ occupy the W-layer. Therefore, this material is recognized as a spin-charge frustrated system. Charge structure was investigated by the electron and x-ray diffraction experiments.[17,18,19] In $LuFe_2O_4$, below 500K, streak-type diffuse scattering was observed along $(1/3\ 1/3\ l)$ lines, and below 320K, spots appear at $(1/3\ 1/3\ 3m + 1/2)$ in the streak lines associated with zigzag modulations. In this pa-

per, we use the hexagonal index, although the space group is $R\bar{3}m$. These experimental results are interpreted as two- and three-dimensional charge orders of electrons. The three-dimensional order of $Fe^{2+}$ and $Fe^{3+}$ was also confirmed by the resonant x-ray scattering technique at Fe $K$-edge.[20] As for the magnetic properties, magnetization in $LuFe_2O_4$ starts to increase around 250K.[21] Neutron diffraction experiments revealed that magnetic Bragg peaks at $(1/3\ 1/3\ m)$ appear and a ferrimagnetic order realizes below this temperature.[22,23,24,25,26] Electric polarization and dielectric anomalies were observed around the three-dimensional charge ordering temperature, although the dielectric constant shows strong dispersive and diffusive nature.[20,27] Several magneto-dielectric phenomena were also reported around the ferrimagnetic ordering temperature.[20,28,29] It is worth noting that these dielectric and magnetic phenomena depend on the rare-earth metal element, $R$, and the oxygen stoichiometry; in $YFe_2O_4$, with decreasing temperature, the three fold-type charge order is changed into a four fold-type one which is extremely sensitive to oxygen deficiency.[30,31,32] These microscopic and macroscopic experiments denote that $3d$ electronic charges are responsible for the dielectric anomalies, and couple strongly with spins.

To elucidate mechanism of dielectric phenomena in $RFe_2O_4$, Yamada and coworkers proposed a model for the three fold-type charge order.[18] This charge-structure model is shown in Fig. 5(a) which will be introduced in more detail in Sect. III. This is a $\sqrt{3} \times \sqrt{3}$ structure in a plane, and along [110], electronic charges are aligned $\cdots Fe^{3+}Fe^{3+}Fe^{2+}\cdots$ in the lower plane and $\cdots Fe^{3+}Fe^{2+}Fe^{2+}\cdots$ in the upper one. That is, electronic charge is polarized between the upper and lower planes, and finite electric dipole moments exist in the W-layer. Based on this polar charge model and the neutron diffraction data, a possible spin structure in the ferrimagnetic ordered phase was proposed.[31]

A number of the experimental results[16,18,20,21,22] and the analyses[17,24,33,34,35] imply that electronic processes and interactions are crucial for novel dielectric properties in this material. In this paper, we present a microscopic theory of electronic structure and magneto-dielectric phenomena in $RFe_2O_4$. We focus on $3d$ electronic structure in a W-layer which is a minimum and main stage for the low-energy elec-
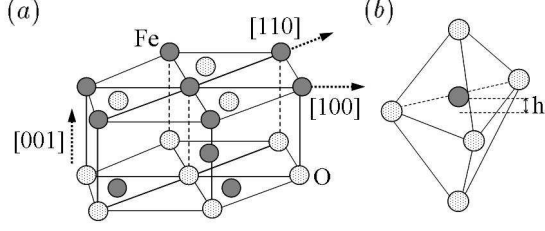
FIG. 1: (a) : A pair of triangular-lattice planes (W-layer). (b) : A FeO$_5$ cluster.

tronic state. We first suggest the orbital degree of freedom in a Fe$^{2+}$ ion, and derive an electronic Hamiltonian in a W-layer. This model consists of the long-range Coulomb interactions and the exchange interaction derived from the generalized $pd$ model. We analyze the charge structure by using the mean-field approximation and the Monte-Carlo (MC) simulation. The three-fold type polar charge order competes with other type non-polar ones, and is stabilized at finite temperature. This is caused by charge fluctuation in a frustrated triangular lattice. We furthermore examine spin structure and coupling between spin ordering and electric polarization. The polar charge order is strongly stabilized below the magnetic ordering temperature. This magneto-dielectric phenomenon is attributed to spin frustration in a triangular lattice. We demonstrate novel electric and magnetic responses which are available to examine the present theoretical scenario. Effects of oxygen deficiency on electric polarization are also studied.

In Sect. II, we derive the model Hamiltonian for electronic structure in a W-layer. In Sect. III, numerical results for the charge structure and electric polarization are presented. Calculated results for the spin structure and the magneto-dielectric responses are shown in Sect. IV. Examined oxygen deficiency effects are introduced in Sect. V. Section VI is devoted to discussion and concluding remarks. Preliminary results for the present study have been published in Refs. 33 and 34. Study of a doubly degenerate orbital model in a honeycomb lattice as an orbital model for $R$Fe$_2$O$_4$ is presented in separate papers.[34,36]

## II. MODEL HAMILTONIAN

We start from the electronic structure in a single Fe ion in the W-layer. This ion is five-fold coordinate with three O ions in the $xy$ plane and two at apices as shown in Fig. 1 (b). We calculate the crystalline-field splitting of the Fe $3d$ orbitals in the FeO$_5$ cluster. Five O ions are replaced by point charges with valence of $-2e$, and their positions are determined by the crystal structure data.[37,38] The hydrogen-like wave functions are adopted for the Fe $3d$ orbitals, and the effective nuclear charge is taken to be $+8$. The split $3d$ orbitals are identified by the irreducible representation in the D$_{3d}$ group: the $d_{3z^2-r^2}$ orbital with A', and two sets of the doubly de-

generate orbitals $(-ad_{zx}+bd_{x^2-y^2},\ ad_{yz}+bd_{xy})$ with E', and $(ad_{x^2-y^2}+bd_{zx},\ -ad_{xy}+bd_{yz})$ with E''. Numerical coefficients $a$ and $b$ satisfy the relation $a^2+b^2=1$. We obtain that the degenerate E' orbitals take the lowest energy with $b=0.89$, and the first excited level is E''. The energy difference between E' and E'', $\Delta E_{E'-E''}$, is about 0.1eV which is smaller than that between E'' and A', $\Delta E_{E''-A'} \sim 0.6$eV. When we see the crystal structure in detail, an Fe ion is not located at center of a O$_5$ cage. Distance between the Fe ion and the O$_3$ plane denoted by $h$ [see Fig. 1 (b)] is about 0.1Å in LuFe$_2$O$_4$.[37,38] We obtain that, with taking $h$ into account, $\Delta E_{E'-E''}$ increases and $\Delta E_{E''-A'}$ decreases. The hybridization effects between Fe $3d$ and O $2p$ orbitals may increase these level separations. However, because of the small value of $\Delta E_{E'-E''}$, we do not exclude a possibility that $(d_{x^2-y^2},\ d_{xy})$ and $(d_{zx},\ d_{yz})$ couple strongly with each other, i.e. $a \sim b$, and that the E'' level is the lowest. In any cases, the lowest orbitals are degenerate. As a result, in Fe$^{3+}$, each orbital is singly occupied, and total spin $S=5/2$ of the high-spin state. On the other hand, in Fe$^{2+}$, one of the degenerate lowest levels is doubly occupied by a hole, and $S=2$. Thus, two fold orbital degeneracy exists in Fe$^{2+}$. This is represented by the orbital pseudo-spin operator defined by

$$\mathbf{T}_i = \frac{1}{2}\sum_{\mu\mu's} d^\dagger_{i\mu s}\sigma_{\mu\mu'}d_{i\mu's}, \tag{1}$$

where $d^\dagger_{i\mu s}$ is the creation operator for an Fe $3d$ hole with orbital $\mu$, spin $s(=\uparrow, \downarrow)$ at site $i$, and $\sigma_{\mu\mu'}$ is the Pauli matrices. In following part of this paper, we assume for simplicity that the two orbitals in the lowest level are $(d_{x^2-y^2}, d_{xy})$, and the index $\mu$ in Eq. (1) takes the two. The $z$ component of the operator $T_i^z$ is $1/2\ (-1/2)$ for the state where a hole occupies the $d_{x^2-y^2}\ (d_{xy})$ orbital. Even in the case where the orbitals in the lowest level are $(d_{zx}, d_{yz})$, the following part of this paper is valid by reinterpreting that the index $\mu$ in Eq. (1) takes $(d_{yz}, d_{zx})$.

We set up the model Hamiltonian for the electronic structure in a W-layer. The $3d$ electrons in the Fe ions and the $2p$ ones in O which hybridizes with Fe $3d$ are introduced. We start from the following generalized $pd$ Hamiltonian,

$$\mathcal{H}_{pd} = \mathcal{H}_d + \mathcal{H}_p + \mathcal{H}_t + \mathcal{H}_V, \tag{2}$$

with

$$\begin{aligned}
\mathcal{H}_d = &\sum_{i\mu\sigma}\varepsilon^d_\mu d^\dagger_{i\mu\sigma}d_{i\mu\sigma} \\
&+\sum_{i\mu}U^d n^d_{i\mu\uparrow}n^d_{i\mu\downarrow} + \frac{1}{2}\sum_{i\mu\neq\mu'\sigma\sigma'}W^d n^d_{i\mu\sigma}n^d_{i\mu'\sigma'} \\
&-\frac{1}{2}\sum_{i\mu\neq\mu'\sigma\sigma'}I^d d^\dagger_{i\mu\sigma}d_{i\mu\sigma'}d^\dagger_{i\mu'\sigma'}d_{i\mu'\sigma}, \tag{3}
\end{aligned}$$
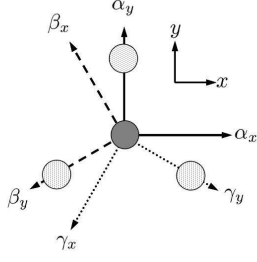
FIG. 2: Three two-dimensional coordinates, $(\alpha_x, \alpha_y)$, $(\beta_x, \beta_y)$ and $(\gamma_x, \gamma_y)$ in a FeO triangular lattice. Filled and dotted circles represent Fe and O ions, respectively.

$$\mathscr{H}_p = \sum_{jv\sigma} \varepsilon_v^p p_{jv\sigma}^\dagger p_{jv\sigma}$$
$$+ \sum_{jv} U^p n_{jv\uparrow}^p n_{jv\downarrow}^p + \frac{1}{2} \sum_{jv \neq v'\sigma\sigma'} W^p n_{jv\sigma}^p n_{jv'\sigma'}^p$$
$$- \frac{1}{2} \sum_{jv \neq v'\sigma\sigma'} I^p p_{jv\sigma}^\dagger p_{jv\sigma'} p_{jv'\sigma'}^\dagger p_{jv'\sigma}, \qquad (4)$$

$$\mathscr{H}_t = \sum_{i\eta\sigma} t^{pd} d_{i\eta_x^2-\eta_y^2\sigma}^\dagger p_{i+\delta_\eta \eta_y \sigma} + \text{H.c.}, \qquad (5)$$

$$\mathscr{H}_V = \left( \sum_{\langle ij \rangle}^{\text{abNN}} V_{\text{abNN}} + \sum_{\langle ij \rangle}^{\text{cNN}} V_{\text{cNN}} + \sum_{\langle ij \rangle}^{\text{cNNN}} V_{\text{cNNN}} \right) n_i^d n_j^d, \qquad (6)$$

where $d_{i\mu\sigma}^\dagger$ is the creation operator for the Fe $3d$ hole with orbital $\mu$ (= $xy$, $x^2 - y^2$, $yz$, $zx$, $3z^2 - r^2$) and spin $\sigma$ (=$\uparrow, \downarrow$) at site $i$, and $p_{jv\sigma}^\dagger$ is for the O $2p$ hole with orbital $v$ (= $x$, $y$, $z$). Number operators are defined by $n_{i\mu\sigma}^d = d_{i\mu\sigma}^\dagger d_{i\mu\sigma}$, $n_{jv\sigma}^p = p_{jv\sigma}^\dagger p_{jv\sigma}$, and $n_i^d = \sum_{\mu\sigma} n_{i\mu\sigma}^d$. A simbol $\delta_\eta$ is a connecting vector between Fe and NN O ions along directin $\eta$. Interactions in a Fe ion are described in the 1st term of Eq. (2), $\mathscr{H}_d$, where the level energy $\varepsilon_\mu^d$, the intra-orbital Coulomb interaction $U^d$, the inter-orbital one $W^d$, and the exchange interaction $I^d$ are considered. Interactions in $\mathscr{H}_p$ are defined in the same way with those in $\mathscr{H}_d$. Hopping of a hole between the nearest neighboring (NN) Fe and O ions in the same plane is described in $\mathscr{H}_t$ with the transfer integral $t^{pd}$. For convenience, we introduce the three two-dimensional coordinates $(\eta_x, \eta_y)$ with $\eta = (\alpha, \beta, \gamma)$, which are obtained by a rotation of the $xy$ axis by $2\pi m_\eta / 3$ with $(m_\alpha, m_\beta, m_\gamma) = (0, 1, 2)$ (see Fig. 2). In each coordinate, we define the operators as

$$\begin{pmatrix} d_{i\eta_x^2-\eta_y^2\sigma} \\ d_{i\eta_x\eta_y\sigma} \end{pmatrix} = \begin{pmatrix} \cos\frac{4\pi}{3}m_\eta & \sin\frac{4\pi}{3}m_\eta \\ -\sin\frac{4\pi}{3}m_\eta & \cos\frac{4\pi}{3}m_\eta \end{pmatrix} \begin{pmatrix} d_{ix^2-y^2\sigma} \\ d_{ixy\sigma} \end{pmatrix}, \quad (7)$$

and

$$\begin{pmatrix} p_{i\eta_x\sigma} \\ p_{i\eta_y\sigma} \end{pmatrix} = \begin{pmatrix} \cos\frac{2\pi}{3}m_\eta & \sin\frac{2\pi}{3}m_\eta \\ -\sin\frac{2\pi}{3}m_\eta & \cos\frac{2\pi}{3}m_\eta \end{pmatrix} \begin{pmatrix} p_{ix\sigma} \\ p_{iy\sigma} \end{pmatrix}. \quad (8)$$

In the bond direction $\eta$, the $d_{\eta_x^2-\eta_y^2}$ and $p_{\eta_y}$ orbitals compose the $\sigma$ bond. The inter-site Coulomb interactions between Fe
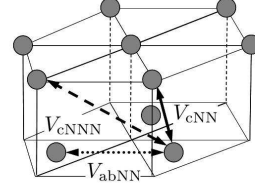


FIG. 3: Inter-site Coulomb interactions between Fe ions. Solid, broken and dotted arrows represent interactions between the nearest neighbor ($V_{\text{cNN}}$), the next nearest neighbor ($V_{\text{abNN}}$) and the third neighbor ($V_{\text{cNNN}}$) Fe-Fe bonds, respectively.

ions are taken into account in the last term of Eq. (2), i.e. $\mathscr{H}_V$. We consider the largest three interactions in the W-layer as shown in Fig. 3: the inter-plane NN interaction ($V_{\text{cNN}}$), the intra-plane NN one ($V_{\text{abNN}}$) and the inter-plane next NN one ($V_{\text{cNNN}}$). This is because (1) these Coulomb interactions are a minimum set which reproduces the three-types of charge structures observed experimentally, and (2) a distance between the 4th neighbor Fe ions in the W-layer is comparable to that between the NN W-layers. This will be discussed in Sect. III in more detail. Summations in $\mathscr{H}_V$ take the three kinds of pairs. When the $1/r$-type Coulomb interaction is assumed, we obtain $V_{\text{cNN}}/V_{\text{abNN}} = 1.2$ and $V_{\text{cNNN}}/V_{\text{abNN}} = 0.77$ for LuFe$_2$O$_4$. By introducing the pseudo-spin operator $Q_i^z$ for charge degree of freedom, $\mathscr{H}_V$ is rewritten as an antiferromagnetic Ising model

$$\mathscr{H}_V = \left( \sum_{\langle ij \rangle}^{\text{cNN}} V_{\text{cNN}} + \sum_{\langle ij \rangle}^{\text{abNN}} V_{\text{abNN}} + \sum_{\langle ij \rangle}^{\text{cNNN}} V_{\text{cNNN}} \right) Q_i^z Q_j^z, \quad (9)$$

where a constant term is omitted. The operator $Q_i^z$ takes $1/2$ and $-1/2$ for Fe$^{3+}$ and Fe$^{2+}$, respectively. The charge conservation is imposed by a relation $\sum_i Q_i^z = 0$.

Based on the extended $pd$ Hamiltonian $\mathscr{H}_{pd}$, we derive the effective Hamiltonian for the superexchange interactions between NN Fe ions in a plane. This interaction arises from virtual hopping of holes between Fe ions. The Hamiltonian is derived by the 4th order projection-perturbation procedure in terms of the hopping term $\mathscr{H}_{pd}$. Following two exchange processes are considered:

$$d^M p^0 d^N \rightarrow d^{M+1} p^0 d^{N-1} \rightarrow d^M p^0 d^N, \qquad (10)$$

and

$$d^M p^0 d^N \rightarrow d^{M-1} p^2 d^{N-1} \rightarrow d^M p^0 d^N, \qquad (11)$$

where we adopt the hole picture, and $M$ and $N$ represent the numbers of holes. These are termed the $dd$- and $dpd$- processes, respectively, from now on. Here, we present the outline of derivation, and details are given in Appendix A. A general form of the Hamiltonian is

$$\mathscr{H}_J = \hat{P}\mathscr{H}_t \frac{1}{E_i - \mathscr{H}_0} \hat{Q}\mathscr{H}_t \frac{1}{E_i - \mathscr{H}_0} \hat{Q}\mathscr{H}_t \frac{1}{E_i - \mathscr{H}_0} \hat{Q}\mathscr{H}_t \hat{P}, \quad (12)$$

where $\hat{P}$ is the projection operator for the $d^5$ ($d^4$) high-spin states in $Fe^{3+}$ ($Fe^{2+}$), $\hat{Q} = 1 - \hat{P}$, and $E_i$ is the initial-state energy. Many body effects of $\mathscr{H}_V$ in the intermediate states are considered approximately; we assume that the intermediate-state energies for $d^{M+1}p^0 d^{N-1}$ [see Eq.(10)] are higher than the initial- and final-state energies by a constant energy parameter $\widehat{V}$, which is of the order of the inter-site Coulomb interaction. Then, we set $\mathscr{H}_0 = \mathscr{H}_d + \mathscr{H}_p + \widehat{V}$. We interpret that effects of $\mathscr{H}_V$ in other intermediate states are included in the charge-transfer energy, $\Delta_{CT}$, between the $d_{\eta_x^2 - \eta_y^2}$ and $p_{\eta_y}$ orbitals. The obtained Hamiltonian $\mathscr{H}_J$ is classified by valences of Fe ions in the initial states, i.e. $Fe^{m+}$-$Fe^{n+}$ where $n$ and $m$ take 2 and 3, and electron configurations in the intermediate states denoted by $k$. The Hamiltonian is given as

$$\mathscr{H}_J = \sum_{(mn)\, k} \mathscr{H}^{(mn)-k}. \tag{13}$$

All possible intermediate states $k$ are taken into account in Eq. (13) which consists of 6 terms in $\mathscr{H}^{(22)-k}$ and $\mathscr{H}^{(23)-k}$, and 4 terms in $\mathscr{H}^{(33)-k}$. Explicit formulae of all terms are presented in Appendix A. Here, we show some representative terms:

$$\mathscr{H}^{(22)-1} = J^{(22)-1} \sum_{\langle ij \rangle} (\mathbf{I}_i \cdot \mathbf{I}_j + 6) \left( \frac{1}{2} - 2\tau_{i\eta_i} \tau_{j\eta_j} \right)$$
$$\times \left( \frac{1}{2} - Q_i^z \right) \left( \frac{1}{2} - Q_j^z \right), \tag{14}$$

$$\mathscr{H}^{(23)-1} = J^{(23)-1} \sum_{\langle ij \rangle} \left( \mathbf{J}_i \cdot \mathbf{I}_j + \frac{15}{2} \right) \left( \frac{1}{2} - \tau_{j\eta_j} \right)$$
$$\times \left( \frac{1}{2} + Q_i^z \right) \left( \frac{1}{2} - Q_j^z \right), \tag{15}$$

$$\mathscr{H}^{(33)-1} = J^{(33)-1} \sum_{\langle ij \rangle} \left( \mathbf{J}_i \cdot \mathbf{J}_j - \frac{25}{4} \right)$$
$$\times \left( \frac{1}{2} + Q_i^z \right) \left( \frac{1}{2} + Q_j^z \right). \tag{16}$$

We define the spin operators $\mathbf{I}_i$ and $\mathbf{J}_i$ for $Fe^{2+}$ and $Fe^{3+}$ with amplitudes of 2 and 5/2, respectively. The orbital operator is redefined in the ($\eta_x$, $\eta_y$) coordinate as

$$\tau_{i\eta} = T_i^z \cos \left( \frac{2\pi}{3} m_\eta \right) + T_i^x \sin \left( \frac{2\pi}{3} m_\eta \right). \tag{17}$$

This operator takes 1/2 ($-1/2$), when the $d_{\eta_x^2 - \eta_y^2}$ ($d_{\eta_x \eta_y}$) orbital is occupied by a hole. In a given pair of $i$ and $j$ sites, subscripts $\eta_i$ and $\eta_j$ in $\tau_{i\eta_i}$ and $\tau_{j\eta_j}$ are automatically determined. The exchange constants are defined by $J^{(22)-1} = -t_{ddc}^2/[10\Delta_{(22)-1}]$, $J^{(23)-1} = -2t_{ddc}^2/[25\Delta_{(23)-1}]$, and $J^{(33)-1} = 4t_{ddc}^2/[25\Delta_{(33)-1}]$ where $t_{ddc}$ is the transfer integral between NN Fe ions defined by $t_{ddc} = (t_{pd}^2 \cos \theta)/\Delta_{CT}$ with the Fe-O-Fe bond angle $\theta (= 120°)$. We introduce
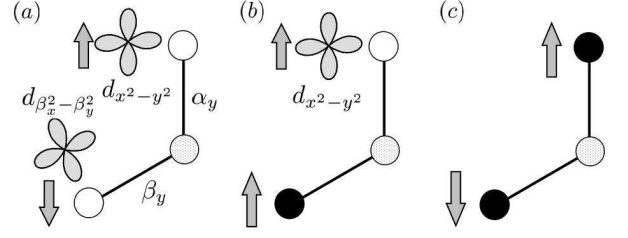


FIG. 4: The lowest-energy spin and orbital configurations for a $Fe^{2+}$-$Fe^{2+}$ bond (a), for $Fe^{3+}$-$Fe^{2+}$ (b), and for $Fe^{3+}$-$Fe^{3+}$ (c). Open, filled and dotted circles represent $Fe^{2+}$, $Fe^{3+}$ and O ions, respectively. Spin and orbital configuration in (a) is energetically close to ferromagnetic spin alignment with $d_{x^2-y^2}$ and $d_{\beta_x \beta_y}$ orbitals.

the intermediate-state energies as $\Delta_{(22)-1} = W^d - I^d + \widehat{V}$, $\Delta_{(23)-1} = \widehat{V}$, and $\Delta_{(33)-1} = U^d + 4I^d + \widehat{V}$. It is worth to note that 1) $\mathscr{H}^{(22)-l}$ is expressed as a product of charge, spin and orbital interactions between given sites $i$ and $j$, and 2) $\mathscr{H}^{(32)-l}$ includes a linear term of the orbital pseudo spin because $Fe^{3+}$ dose not have the orbital degree of freedom.

After all, we obtain the Coulomb- and exchange-interaction Hamiltonian

$$\mathscr{H} = \mathscr{H}_V + \mathscr{H}_J, \tag{18}$$

where $\mathscr{H}_V$ and $\mathscr{H}_J$ are given in Eqs. (9) and (13), respectively. Before going to the numerical results calculated in the Hamiltonian, we briefly mention the energy scales of charge, spin and orbital degrees of freedom, and signs of the exchange interactions. The inter-site Coulomb interactions provide a larger energy scale than the exchange interactions. Thus, the charge sector is frozen at the highest temperature in comparison with spin and orbital ones. This is consistent with the experimental results in $LuFe_2O_4$ where the charge ordering temperature (about 320K) is higher than the spin ordering one (about 250K).[17,18,24] By calculating the exchange energy in a given NN bond, we estimate stable spin and orbital configurations. This is not trivial from the Goodenough-Kanamori rule because of the 120° bond angle. The energy parameter sets for the exchange coupling constant $J^{(mn)-l}$ are determined from the experimental data in $LaFeO_3$,[39,40] and $\mathbf{I}_i$ and $\mathbf{J}_i$ are assumed to be Ising spins. We obtain the spin and orbital configurations for the lowest exchange energies as 1) for a $Fe^{2+}$-$Fe^{2+}$ bond, $I_i^z I_j^z = -4$ (antiferromagnetic) and $\tau_i = \tau_j = 1/2$, which is energetically close to $I_i^z I_j^z = 4$ (ferromagnetic) and $\tau_i = -\tau_j = 1/2$, 2) for $Fe^{3+}$-$Fe^{3+}$, $J_i^z J_j^z = -25/4$ (antiferromagnetic), and 3) for $Fe^{2+}$-$Fe^{3+}$, $I_i^z J_j^z = 5$ (ferromagnetic) and $\tau_i = 1/2$. Schematic views for the stable configurations are presented in Fig. 4. In the neutron scattering experiments, the ferrimagnetic phase indexed as $(1/3\ 1/3\ m)$ appears around 250K. Possible magnetic structures are shown in Fig. 13, which will be explained in more detail later. In this structure, $Fe^{2+}$ ions in the $2Fe^{3+}$-$Fe^{2+}$ (upper) plane are surrounded by six NN $Fe^{3+}$. Thus, the exchange Hamiltonian in this plane

is reduced into a form of $\sum_{\langle ij \rangle}[(1/2) \pm \tau_{i\eta_i}]$ which becomes a constant by using the relation of $\sum_{\langle ij \rangle} \tau_{i\eta_i} = 0$. This relation is also applicable to the $Fe^{2+}$-$Fe^{3+}$ bonds in the $2Fe^{2+}$-$Fe^{3+}$ (lower) plane where three $Fe^{2+}$-$Fe^{3+}$ bonds connecting a $Fe^{2+}$ ion are equivalent [see Fig. 13]. Therefore, the orbital part of the exchange Hamiltonian in this ferrimagnetic phase is mapped onto the following orbital model defined on a $Fe^{2+}$ sublattice;

$$\mathscr{H}_{\text{orb}} = J_{\text{orb}} \sum_i' \left( \tau_{i\beta} \tau_{i+\mathbf{e}_\alpha \gamma} + \tau_{i\gamma} \tau_{i+\mathbf{e}_\beta \alpha} + \tau_{i\alpha} \tau_{i+\mathbf{e}_\gamma \beta} \right), \quad (19)$$

where $(\mathbf{e}_\alpha, \mathbf{e}_\beta, \mathbf{e}_\gamma)$ represent the three unit vectors connecting NN $Fe^{2+}$ sites in a honeycomb lattice. A summation $\sum_i'$ takes $Fe^{2+}$ sites in one of the two sublattices in a honeycomb lattice. The coupling constant $J_{\text{orb}}$ is given by the exchange constants $J^{(nm)-k}$. In this model, it is obtained theoretically that the orbital does not show a conventional long-range order down to very low temperature of the order of $0.005 J_{\text{orb}}$. Therefore, for simplicity, we assume that the pseudo-spin operators for orbital in $\mathscr{H}_J$ are set to be zero in the following calculation. Theoretical study of the orbital model on a honeycomb lattice is presented in separate papers.[34,36]

## III. CHARGE STRUCTURE AND ELECTRIC POLARIZATION

First we focus on the charge structure and the electric polarization by analyzing the inter-site Coulomb interaction term $\mathscr{H}_V$. We apply, at the first stage, the mean-field approximation to $\mathscr{H}_V$, and obtain stable charge structures. The charge conservation is taken into account by adding the chemical potential term, $-V_{\text{ext}} \sum_i Q_i^z$, in the Hamiltonian. We assume that the expectation value $\langle Q_i^z \rangle$ is periodic along the $\langle 110 \rangle$ or $\langle 210 \rangle$ directions, and takes the same amplitude along $\langle \bar{1}10 \rangle$ or $\langle 010 \rangle$, respectively. Periodicity $L$ is taken up to 12. In upper and lower planes, $\langle Q_i^z \rangle$'s are independent and have the same periodicity along the $\langle 110 \rangle$ or $\langle 210 \rangle$ directions. Each solution is characterized by the momentum $\mathbf{q} \equiv (M/2L, M/2L, n)$ or $(M/2L, 0, n)$ where $M$ is the number of nodes of $\langle Q_i^z \rangle$ along the $\langle 110 \rangle$ or $\langle 210 \rangle$ directions, respectively. When a phase difference between $\langle Q_i^z \rangle$'s in the upper and lower planes is $0$ ($\pi$), $n$ takes $0$ ($1/2$). Phase diagram is determined by comparing the free energy. Representative charge structures are shown in Fig. 5. Four types of CO's in this figure, denoted by $CO_{1/3}$, $CO_{1/4}$, $CO_{1/2}$-I and $CO_{1/2}$-II, are characterized by momenta $\mathbf{q} = (1/3, 1/3, 0) \equiv \mathbf{q}_{1/3}$, $(1/4, 1/4, 1/2) \equiv \mathbf{q}_{1/4}$, $(1/2, 1/2, 0) \equiv \mathbf{q}_{1/2\text{-I}}$ and $(1/2, 0, 0) \equiv \mathbf{q}_{1/2\text{-II}}$, respectively. As suggested by Yamada and coworkers, $CO_{1/3}$ shows finite electric polarization due to charge imbalance between the two triangular-lattice planes.[17,18] A ratio of $Fe^{2+}$ and $Fe^{3+}$ is $1:2$ ($2:1$) in the upper (lower) plane. In other charge structures, equal numbers of $Fe^{2+}$ and $Fe^{3+}$ occupy the upper and lower planes, and there is no electric polarization.

Mean-field phase diagram at zero temperature is presented in Fig. 6. The non-polar $CO_{1/2}$-II and $CO_{1/4}$ structures are stable in the regions of $V_{\text{CNN}}/V_{\text{CNNN}} < 2$ and $V_{\text{CNN}}/V_{\text{CNNN}} >$
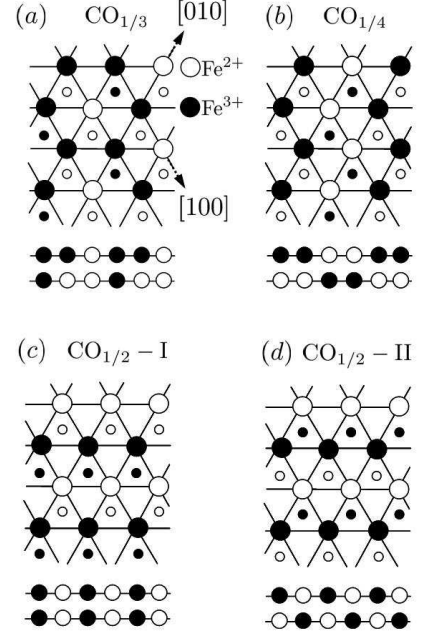


FIG. 5: Charge structures in a W-layer : (a) $CO_{1/3}$, (b) $CO_{1/4}$, (c) $CO_{1/2}$-I, and (d) $CO_{1/2}$-II. Filled and open circles represent $Fe^{3+}$ and $Fe^{2+}$, respectively, and large and small circles are for Fe ions in the upper and lower planes, respectively. Lower panel in each figure is a side view from $[1\bar{1}0]$.

2, respectively. The polar $CO_{1/3}$ structure appears only on the phase boundary where $CO_{1/3}$ is degenerate with $CO_{1/2}$-II and $CO_{1/4}$. Realistic parameter values for $R$Fe$_2$O$_4$ correspond to a shaded area in Fig. 6. We fix a value of $V_{\text{cNN}}/V_{\text{abNN}}$ to be 1.2, as shown by a dashed line in Fig. 6, and calculate finite-temperature phase diagram (Fig. 7). The polar $CO_{1/3}$ is stabilized in a wide region between $CO_{1/4}$ and the $CO_{1/2}$-II.

Beyond the mean-field calculation, we examine the charge structure in finite temperature by using the MC simulation. To avoid a trap of a simulation in local minima, we adopt the multi-canonical MC (MUMC) method.[41] Simulations are performed on a paired triangular lattice of $L \times L \times 2 (\equiv 2N)$ ($L = 6$ and 12) sites with the periodic-boundary condition in the $ab$ plane. We use $6 \times 10^6$ MC steps to obtain a histogram in the MUMC method and $16 \times 10^6$ MC steps for measurement. We calculate the charge correlation function and the electric polarization $P$ defined by

$$N(\mathbf{q}) = \frac{1}{(2N)^2} \sum_{ij} \langle Q_i^z Q_j^z \rangle e^{-i\mathbf{q} \cdot (\mathbf{r}_i - \mathbf{r}_j)}, \quad (20)$$

$$P = \langle p^2 \rangle^{1/2}. \quad (21)$$

with

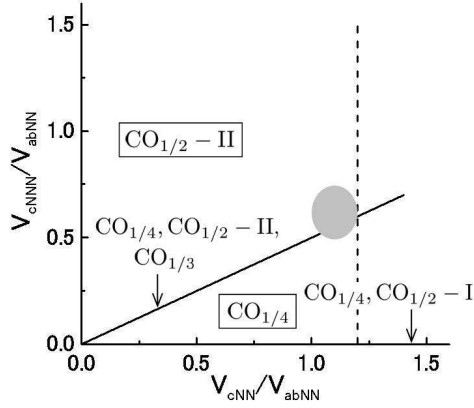$$p = \frac{1}{N} \left( \sum_i^u - \sum_i^l \right) Q_i^z, \quad (22)$$

FIG. 6: Mean-field phase diagram for charge order at zero temperature. Three charge structures, $CO_{1/4}$, $CO_{1/2}$-II, and $CO_{1/3}$, are degenerate on a line of $V_{cNN} = 2V_{cNNN}$, and the two, $CO_{1/4}$ and $CO_{1/2}$-I, are degenerate on a line of $V_{cNN} = 0$. Shaded area corresponds to a region for $R\mathrm{Fe_2O_4}$. Phase diagram in finite temperatures, shown in Fig. 7, is calculated on broken line.
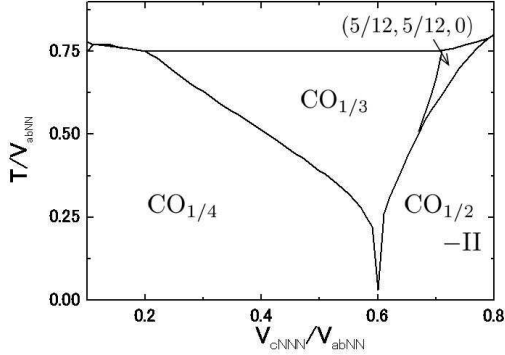


FIG. 7: Mean-field phase diagram for charge structure in finite temperatures. The Coulomb interaction $V_{cNN}/V_{abNN}$ is chosen to be 1.2.

where $r_i$ is a position of site $i$, and $\sum_i^{u(l)}$ represents a summation of site $i$ in the upper (lower) plane.

The charge correlation functions at $V_{cNNN}/V_{abNN} = 0.58$, 0.6 and 0.62 are presented in Fig. 8. At $V_{cNNN}/V_{abNN} = 0.6$, $N(\mathbf{q}_{1/3})$ shows a hump around $\widetilde{T} \equiv T/V_{abNN} = 0.18$ and keeps a finite value down to the low temperature limit. From the specific heat data, we identify $\widetilde{T} = 0.18$ corresponds to the charge-ordering temperature. In the both cases of $V_{cNNN}/V_{abNN} = 0.58$ and 0.62, $N(\mathbf{q}_{1/3})$ is dominant in high temperatures, starts to decrease around $\widetilde{T} = 0.2$ and disappears at the lowest temperature. On the contrary, the charge correlation $N(\mathbf{q}_{1/2-II})$ and $N(\mathbf{q}_{1/4})$ grow up around $\widetilde{T} = 0.05$, and increase with decreasing temperature. These results and the specific heat data imply that the charge order at $\mathbf{q}_{1/3}$ is changed into the other type of charge order at $\mathbf{q}_{1/4}$ ($\mathbf{q}_{1/2-I}$) around $\widetilde{T} = 0.04$ (0.045) for $V_{cNNN}/V_{abNN} = 0.58$ (0.62). Tem-
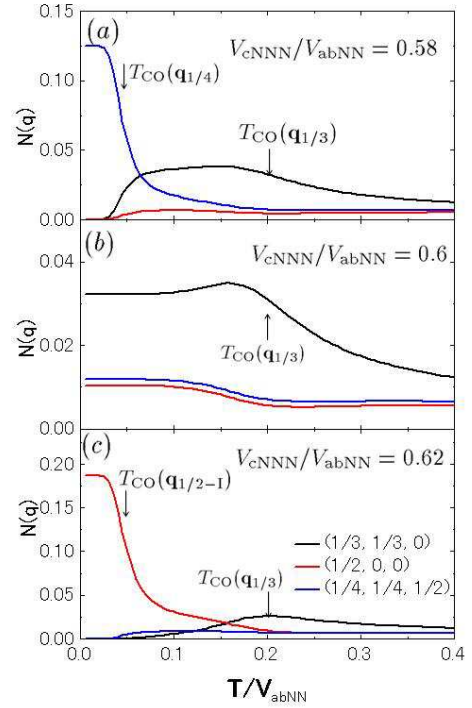


FIG. 8: Charge correlation functions $N(\mathbf{q})$ at $V_{cNNN}/V_{abNN} = 0.60$ (a), 0.58 (b) and 0.62 (c) calculated in $\mathscr{H}_V$. The Coulomb interaction $V_{cNN}/V_{abNN}$ is chosen to be 1.2.
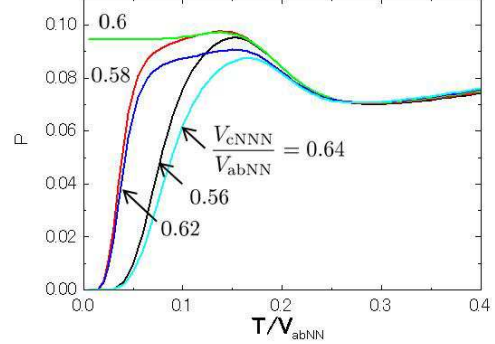


FIG. 9: Electric polarization $P$ as a functions of $V_{cNNN}/V_{abNN}$ calculated in $\mathscr{H}_V$. The Coulomb interaction $V_{cNN}/V_{abNN}$ is chosen to be 1.2.

perature dependence of $P$ at several values of $V_{cNNN}/V_{abNN}$ is presented in Fig. 9. At $V_{cNNN}/V_{abNN} = 0.6$, $P$ remains down to the low temperature limit. Apart from $V_{cNNN}/V_{abNN} = 0.6$, $P$ starts to decrease at the temperature where $N(\mathbf{q}_{1/2-II})$ and $N(\mathbf{q}_{1/4})$ grow up, and disappears at the lowest temperature. These results obtained by the MUMC method are qualitatively consistent with the ones in the mean-field calculation.

The polar charge structure characterized by $\mathbf{q}_{1/3}$ and the transition to the another structure characterized by $\mathbf{q}_{1/4}$ at $V_{cNNN}/V_{abNN} < 0.6$ are consistent with the experimental results. In LuFe$_2$O$_4$, charge order indexed as $(1/3\ 1/3\ 3m+$
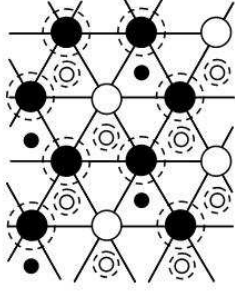
FIG. 10: Two-sublattice structure in the $CO_{1/3}$ phase. Amplitude of the mean-field at Fe sites surrounded by broken circles is $0.9V_{abNN}$ and that at other sites is $2.1V_{abNN}$.

1/2) appears around 350K and remains, at least, down to around 20K.[17] On the other hand, in $YFe_2O_4$, charge order indexed as $(1/3\ 1/3\ 3m+1/2)$ observed at room temperature is changed into the one as $(1/4\ 1/4\ 3/4)$ around 250K.[31,32] We suppose that different rare-earth metal ions slightly change ratio of the Coulomb potentials, and $LuFe_2O_4$ ($YFe_2O_4$) corresponds to the parameter region of $V_{cNNN}/V_{abNN} \approx 0.6$ ($V_{cNNN}/V_{abNN} < 0.6$) in the present calculation.

Stability of the $CO_{1/3}$ phase is attributed to large thermal fluctuation in the geometrically frustrated lattice. A key issue is the two-sublattice structure in this charge ordered phase (see Fig. 10):[43] $Fe^{2+}$ ions in the $2Fe^{2+}$-$Fe^{3+}$ (lower) plane and $Fe^{3+}$ in the $Fe^{2+}$-$2Fe^{3+}$ (upper) one belong to a sublattice termed A. Other Fe ions belong to another sublattice termed B. All in-plane NN ions of a site in the sublattice B have an opposite valence. On the other hand, a site on the sublattice A is surrounded by three NN $Fe^{2+}$ and three NN $Fe^{3+}$ in the plane. Therefore, the Coulomb potentials at these sites from the in-plane NN ions are canceled out, and charge fluctuation is able to occur easily without loss of $V_{abNN}$. It is obtained in the numerical calculation that an amplitude of the mean-field on the sublattice A is $0.9V_{abNN}$ at low temperature which is much less than that on the sublattice B, $2.1V_{abNN}$. Large charge fluctuation at the sites grows up with increasing temperature, and contributes to the entropy gain at finite temperature. On the contrary, in the $CO_{1/2}$-II and $CO_{1/4}$ structures, all $Fe^{2+}$ ($Fe^{3+}$) are equivalent and charge fluctuation is weaker than that in the sublattice A of $CO_{1/3}$. This is the reason why the polar charge order characterized by $(1/3, 1/3, 0)$ is more stable than other charge structures in finite temperatures.

Let us focus on the charge structure in low temperatures in more detail. As shown in Figs. 8 (b) and 9, saturated values of $N(\mathbf{q}_{1/3})$ and $P$ in $V_{cNNN}/V_{abNN}$=0.6 at the low temperature limit are 0.032 and 0.094, respectively, which are smaller than the values expected from the ideal $CO_{1/3}$ phase, 0.056 and 0.33 respectively. This implies that the charge configuration at low temperature in $V_{cNNN}/V_{abNN} = 0.6$ is not the ideal $CO_{1/3}$ state. We analyze the probability histogram in the MUMC simulation, and examine the charge configurations realized in lowest temperatures. These are classified into the following three configurations: the polar $CO_{1/3}$ structure shown in Fig. 5 (a), partially polarized charge structures

characterized by the momentum $\mathbf{q}_{1/3}$, termed $CO_A$, and non-polar structures termed $CO_B$. Detailed structures of $CO_A$ and $CO_B$ are shown in Appendix B. In $CO_A$, the polarization is $P = N/3 - n\sqrt{N}$ with an integer number $n$ satisfying a relation of $0 \le n \le 2\sqrt{N}/3$. Degeneracy of a sum of these configurations is of the order of $\sum_n\ _{2\sqrt{N}/3}C_n \sim 2^{\sqrt{N}}$. As for the $CO_B$ state, degeneracy of the configuration is also of the order of $2^{\sqrt{N}}$. Because of the coexistence of these charge structures, the saturated values of $P$ and $N(\mathbf{q}_{1/3})$ are smaller than the expected values from the ideal $CO_{1/3}$ state. This tendency is remarkable in the large system size, as shown in Fig. 9.

This coexistence of the polar and non-polar CO states implies that the full polarization expected from the ideal $CO_{1/3}$ state is realized by additional weak interactions. The long-range Coulomb interactions between the NN W-layers is one of the candidates. This scenario is plausible, since, in $LuFe_2O_4$, the electric polarization appears around the three-dimensional charge-ordering temperature.[20,27] We examine effects of the inter W-layer Coulomb interaction based on a model where two W-layers stacked along the $c$ axis are coupled by the Coulomb interaction. Saturated values of $N(\mathbf{q}_{1/3})$ and $P$ at low temperature are identical to the expected values from the ideal polar $CO_{1/3}$ state. Roles of the exchange interaction as another candidate to lift the degeneracy are examined in the next section.

## IV. SPIN STRUCTURE AND MAGNETO-ELECTRIC EFFECT

In this section, we introduce spin degree of freedom and examine coupling between the electric polarization and the magnetic ordering. The Hamiltonian $\mathscr{H}_V + \mathscr{H}_J$ is analyzed by utilizing the MUMC method in a $6{\times}6{\times}2$-site cluster. The spin operators $\mathbf{I}_i$ and $\mathbf{J}_i$ in $\mathscr{H}_J$ are assumed to be Ising spins because of the strong magnetic anisotropy observed in $RFe_2O_4$.[24] The energy parameters in the Hamiltonian are chosen to be $U^d = 7.8$, $W^d = 6.2$, $I^d = 0.8$, $U^p = 4.1$, $W^p = 2.9$, $I^p = 0.6$, $t^{pd} = 1.8$, $\Delta_{CT} = 3$ and $\widehat{V} = 1$ in a unit of $V_{abNN}$. These are determined from the experimental date in $LaFeO_3$.[39,40] In this section, the orbital pseudo-spin operators in $\mathscr{H}_J$ are set to be zero, as explained in Sect. II. In particular, we focus on a parameter region around $V_{cNNN}/V_{abNN} = 0.6$, where $CO_{1/3}$ is seen down to the lowest temperature in Fig. 7, and that around 0.58-0.59, where the transition from $CO_{1/3}$ to $CO_{1/4}$ is shown in Fig. 7.

Temperature dependences of the charge correlation function, the spin correlation function defined by

$$S(\mathbf{q}) = \frac{1}{(2N)^2}\sum_{ij}\langle K_i^z K_j^z\rangle e^{-i\mathbf{q}\cdot(\mathbf{r}_i-\mathbf{r}_j)}, \quad (23)$$

where $K_i^z = I_i^z$ ($J_i^z$) for $Fe^{2+}$ ($Fe^{3+}$), and the electric polarization are calculated. Results at $V_{cNNN}/V_{abNN} = 0.60$ and 0.59 are shown in Figs. 11 and 12, respectively. For comparison, we also plot the data obtained in $\mathscr{H}_V$. At $V_{cNNN}/V_{abNN} = 0.6$, three characteristic temperatures, $\widetilde{T} = 0.2$, 0.085 and 0.015,
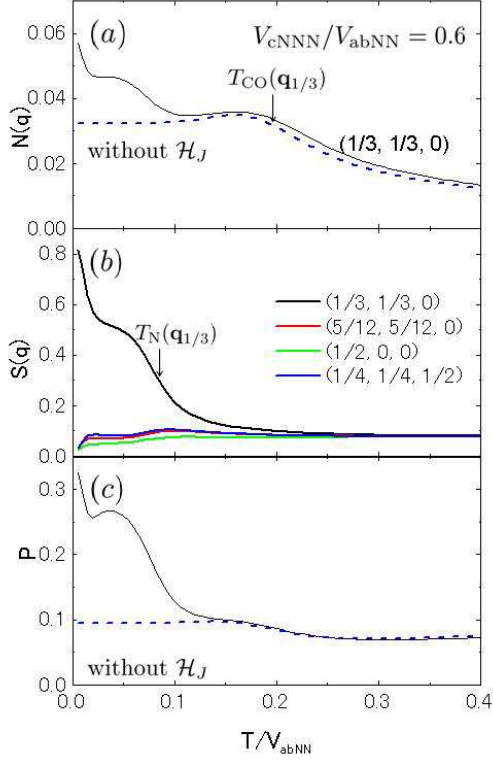
FIG. 11: Charge correlation functions N($\mathbf{q}$) (a), spin correlation functions $S(\mathbf{q})$ (b), and electric polarization $P$ (c) calculated in $\mathscr{H}_V + \mathscr{H}_J$. Dashed lines in (a) and (c) are results obtained in $\mathscr{H}_V$. Parameters are chosen to be $V_{cNN}/V_{abNN} = 1.2$ and $V_{cNNN}/V_{abNN} = 0.60$.
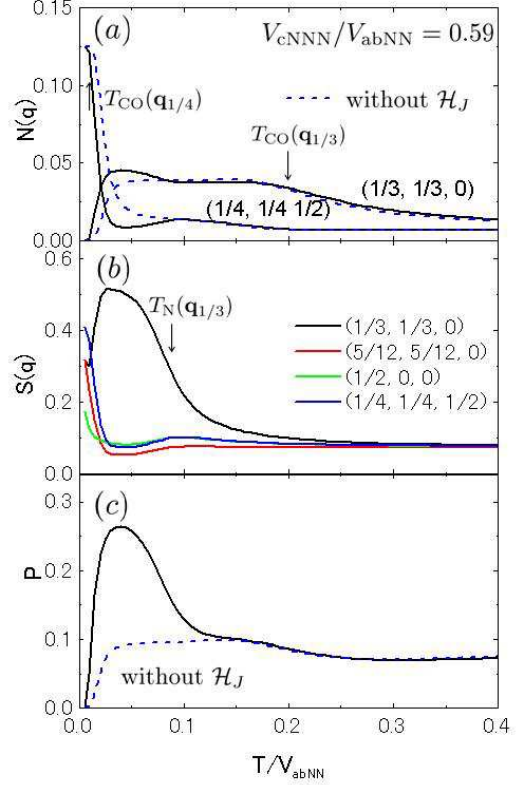


FIG. 12: Charge correlation functions $N(\mathbf{q})$ (a), spin correlation functions $S(\mathbf{q})$ (b), and electric polarization $P$ (c) calculated in $\mathscr{H}_V + \mathscr{H}_J$. Dashed lines in (a) and (c) are results obtained in $\mathscr{H}_V$. Parameters are chosen to be $V_{cNN}/V_{abNN} = 1.2$ and $V_{cNNN}/V_{abNN} = 0.59$.

are seen in $N(\mathbf{q}_{1/3})$. The highest one, $0.2[\equiv T_{CO}(\mathbf{q}_{1/3})]$, corresponds to the charge ordering temperature for $CO_{1/3}$. Other two are the magnetic ordering ones at momentum $\mathbf{q}_{1/3}$. At $\widetilde{T} = 0.085[\equiv T_N(\mathbf{q}_{1/3})]$ and 0.015, spins in the $Fe^{2+}$-$2Fe^{3+}$ and $2Fe^{2+}$-$Fe^{3+}$ planes in $CO_{1/3}$ (see Fig. 5) start to order, respectively. This double-magnetic transition may be an artifact in the present model where the inter-plane exchange interactions are neglected, and spins in the upper and lower planes are independent with each other. We expect that the inter-plane exchange interactions are much smaller than the in-plane ones. This is because, when electrons in the $d_{xy}$ and $d_{x^2-y^2}$ orbitals are concerned, there are no exchange paths between Fe ions in an inter-plane NN bond. When higher-order exchange processes and/or contributions from other $d$ orbitals are taken into account, weak inter-plane interactions may unify the double transition in the present calculation. As shown in Fig. 11, the charge correlation function at $\mathbf{q}_{1/3}$ and the polarization increase at $\widetilde{T} = 0.085$ and 0.014. Results clearly show that magnetic ordering enhances stability of the polar $CO_{1/3}$ phase. In the low temperature limit, $N(\mathbf{q}_{1/3})$ and $P$ take 0.056 and 0.33 respectively, which are the ideal values in $CO_{1/3}$. At $V_{cNNN}/V_{abNN} = 0.59$ (Fig. 12), a weak shoulder in $N(\mathbf{q}_{1/3})$ around $\widetilde{T} = 0.2$ corresponds to the charge ordering for $CO_{1/3}$. Sequential charge ordering transition occurs from $CO_{1/3}$ to $CO_{1/4}$ around $\widetilde{T} = 0.015$ $[\equiv T_{CO}(\mathbf{q}_{1/4})]$,

which is lower a little than the result in $\mathscr{H}_V$. Magnetic order at $\mathbf{q}_{1/3}$ appears around $\widetilde{T} = 0.1[\equiv T_N(\mathbf{q}_{1/3})]$. Below $T_{CO}(\mathbf{q}_{1/4})$, magnetic structure is also changed; the spin correlation functions at $\mathbf{q}_{1/4}$ and $(5/12, 5/12, 0)$ become dominant. It is also shown, in this parameter, that the electric polarization is enhanced in the $CO_{1/3}$ phase. A similar temperature dependence is obtained in $V_{abNN}/V_{cNN} = 0.61$, where the $CO_{1/2}$-II phase appears in low temperatures instead of $CO_{1/4}$.

Low temperature charge and spin structures at $V_{cNNN}/V_{abNN}=0.6$ are shown in Fig. 13(a). Charge structure is identified to be $CO_{1/3}$. Spins at $Fe^{3+}$ in the $Fe^{2+}$-$2Fe^{3+}$ (upper) plane and those at $Fe^{2+}$ in the $2Fe^{2+}$-$Fe^{3+}$ (lower) one are aligned antiferromagnetically. On the other hand, spin directions at $Fe^{2+}$ in the $Fe^{2+}$-$2Fe^{3+}$ plane and at $Fe^{3+}$ in the $2Fe^{2+}$-$Fe^{3+}$ one are not determined uniquely. We note that the spin structure in the $Fe^{3+}$-$2Fe^{2+}$ (lower) plane is sensitive to the parameter values in $\mathscr{H}_J$. The structures shown in Figs. 13(a) and (b) are almost degenerate with each other. The numerical results presented in this paper are obtained in the parameter sets where the spin structure in Fig. 13(a) is obtained. However, qualitative difference for the results in the two parameter sets is not seen. It is also true that essence of the coupling between the spin ordering and the electric polarization shown in Fig. 11 does not depend on the detailed parameter values. Since the antiferromagnetic interaction
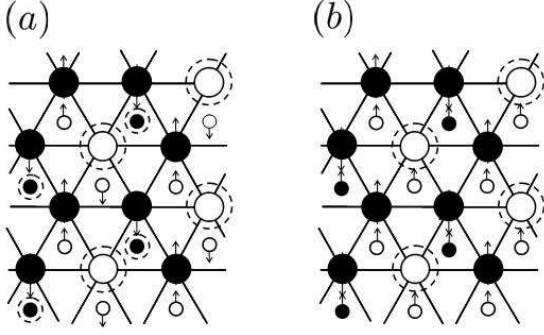
FIG. 13: Charge and spin structures in the polar $CO_{1/3}$ phase at $V_{cNNN}/V_{abNN} = 0.6$. Filled and open circles represent $Fe^{3+}$ and $Fe^{2+}$, respectively, and large and small circles are for Fe ions in the upper and lower planes, respectively. Arrows represent spin directions. At Fe sites surrounded by broken circles, spin directions are not determined uniquely. Spin structures in (a) and (b) are almost degenerate.
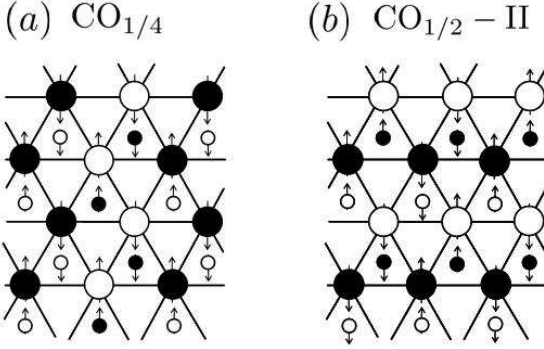


FIG. 14: Charge and spin structure at $V_{cNNN}/V_{abNN} = 0.59$ (a), and that at 0.61 (b).



FIG. 15: Magnetic-field effect in charge correlation function $N(\mathbf{q})$ (a), and electric polarization $P$ (b). Parameters are chosen to be $V_{cNN}/V_{abNN} = 1.2$ and $V_{cNNN}/V_{abNN} = 0.6$. Inset of (b) shows magnetic-field dependence of the electric polarization at $\widetilde{T} = 0.05$.

between NN $Fe^{3+}$-$Fe^{3+}$ bonds in the $2Fe^{3+}$-$Fe^{2+}$ (upper) plane is robust, $Fe^{2+}$ spins are surrounded by three up and three down spins in their NN $Fe^{3+}$ sites. Therefore, spin directions in $Fe^{2+}$ are not determined uniquely as explained above. Because the number of these sites is $N/3$, there is a macroscopic number of degenerate spin states of the order of $2^{N/3}$ which contributes to the entropy gain in finite temperatures. This is a kind of partially disordered phase, which has been examined in the antiferromagnetic Ising model on a triangular lattice.[42] In the present case, spins in $Fe^{2+}$ and $Fe^{3+}$ are inequivalent, i.e. $S = 2$ and $5/2$, and this partial disordered state becomes more stable in comparison with that in the conventional Ising model. Since this spin structure is realized in the $CO_{1/3}$ structure and the spin entropy is larger than the charge entropy in the non-polar and partially-polar charge ordered phases, i.e. $CO_A$ and $CO_B$, the polar $CO_{1/3}$ is reinforced through the spin-charge coupling in the exchange Hamiltonian. This is a kind of "order from fluctuation" mechanism, and, in the present spin-charge coupled system, a ferroelectric order is stabilized
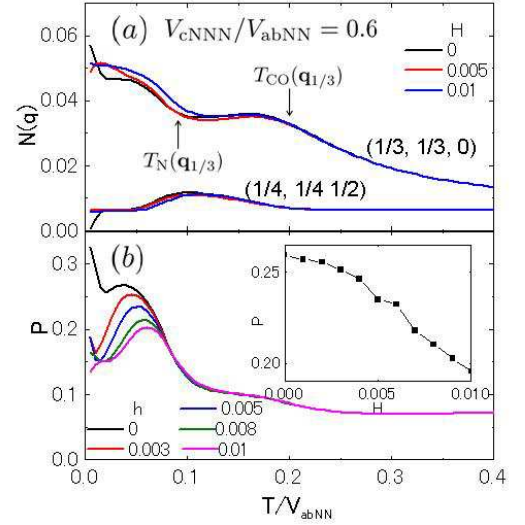
by spin fluctuation. This phenomenon is not expected in $CO_{1/2}$-I, $CO_{1/2}$-II and $CO_{1/4}$. Low temperature charge and spin structures in $V_{cNNN}/V_{abNN} = 0.59$ and $0.61$ are shown in Fig. 14. In both cases, all spins in NN $Fe^{2+}$-$Fe^{2+}$ and $Fe^{3+}$-$Fe^{3+}$ bonds are aligned antiferromagnetically. There are a number of degenerate spin states; for example, when all spins on a chain along [110] in $CO_{1/2}$-II are flipped, the exchange energy is not changed. However, this spin degeneracy is of the order of $2^{\sqrt{N}}$, which is smaller than $O(2^{N/3})$ in $CO_{1/3}$.

In a remaining part of this section, we examine responses to the electric and magnetic fields in the present novel spin-charge coupled system. First we pay our attention to the magnetic-field effect by introducing the Zeeman term of the Hamiltonian

$$\mathcal{H}_H = H \sum_i K_i^z, \qquad (24)$$

where $K_i^z = I_i^z$ or $J_i^z$ for $Fe^{2+}$ or $Fe^{3+}$, respectively, and $H$ is the magnetic field. The Hamiltonian $\mathcal{H}_V + \mathcal{H}_J + \mathcal{H}_H$ is analyzed by utilizing the MUMC method in a $6 \times 6 \times 2$-site cluster. Magnetic field dependence of the electric polarization and the charge correlation functions at $V_{cNNN}/V_{abNN} = 0.6$ and $0.59$ are presented in Figs. 15 and 16, respectively. Temperature in Fig. 15 is chosen to be $\widetilde{T} = 0.05$, which is below the Néel temperature $T_N(\mathbf{q}_{1/3})$, and those in Fig. 16 are $\widetilde{T} = 0.05$ and $0.01$, which are between $T_N(\mathbf{q}_{1/3})$ and the charge ordering temperature of $CO_{1/4}$ $[T_{CO}(\mathbf{q}_{1/4})]$, and below $T_{CO}(\mathbf{q}_{1/4})$, respectively. When $V_{abNN}$ is taken to be 1eV, magnetic field $H/V_{abNN} = 0.01$ corresponds to about 100Tesla. In the magnetically ordered $CO_{1/3}$ phases at $V_{cNNN}/V_{abNN} = 0.6$ and $0.59$, applying the magnetic field reduces the electric polarization. On the other hand, in the antiferromagnetic $CO_{1/4}$ phase at
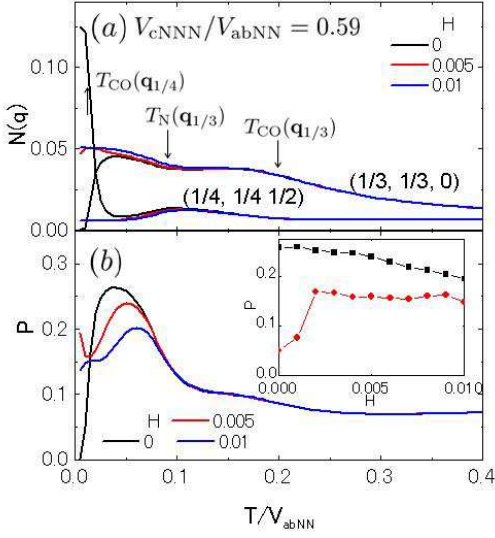
FIG. 16: Magnetic-field effect in charge correlation function $N(\mathbf{q})$ (a), and electric polarization $P$ (b). Parameters are chosen to be $V_{cNN}/V_{abNN} = 1.2$ and $V_{cNNN}/V_{abNN} = 0.59$. Inset of (b) shows magnetic-field dependence of the electric polarization. Solid circles and squares are calculated at $\widetilde{T} = 0.01$ and $0.05$, respectively.
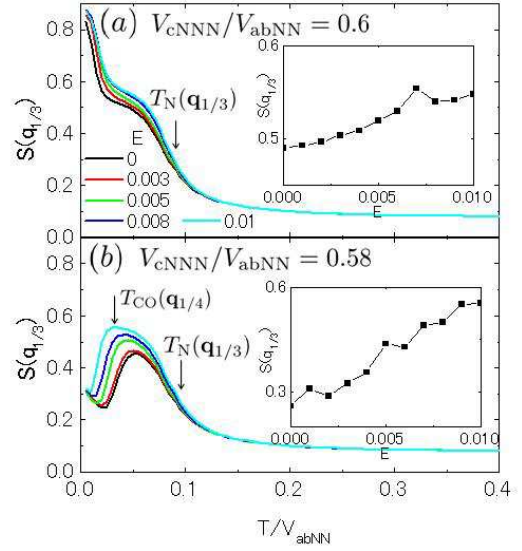


FIG. 17: Electric-field effect of spin correlation function $S(\mathbf{q})$ at $\mathbf{q}_{1/3}$. Parameters are chosen to be $V_{cNNN}/V_{abNN} = 0.6$ (a) and $0.58$ (b) with $V_{cNN}/V_{abNN} = 1.2$. Insets show electric-field dependence of $S(\mathbf{q}_{1/3})$. Temperatures are $\widetilde{T} = 0.05$ in (a), and $0.03$ in (b).

$V_{cNNN}/V_{abNN} = 0.59$ [see $T < T_{CO}(\mathbf{q}_{1/4})$ in Fig. 16(b)], the electric polarization is induced by applying the magnetic field. At the same time, the charge correlation function $N(\mathbf{q}_{1/3})$ increases and $N(\mathbf{q}_{1/4})$ decreases. Similar results are obtained at $V_{cNNN}/V_{abNN} = 0.61$, where the $CO_{1/2-II}$ phase collapses and the electric polarization appears below $\widetilde{T} = 0.015$ by applying the magnetic field. Thus, opposite magnetic-field effects are obtained in the magnetically ordered $CO_{1/3}$ phase and the antiferromagnetic $CO_{1/4}$ and $CO_{1/2-II}$ phases.

We, first, pay our attention to the negative magnetic-field effect in the magnetically ordered $CO_{1/3}$ phase. As explained in Sect. III, the three charge structures, the polar $CO_{1/3}$, the partially polar $CO_A$ and the non-polar $CO_B$, coexist at $H = 0$. Among the three, the polar $CO_{1/3}$ is a dominant structure, because of the large spin entropy due to the spin degeneracy of the order of $2^{N/3}$. By applying the magnetic field, these $N/3$ spins are aligned to be parallel to the magnetic field, and the macroscopic spin degeneracy is lifted. On the other hand, in both the non-polar $CO_B$ and the partially polar $CO_A$, a macroscopic degeneracy in the charge configuration, which is of order of $2^{\sqrt{N}}$, survives under the magnetic field. As the result, the charge entropy in $CO_A$ and $CO_B$ overcomes the spin one in $CO_{1/3}$, and $P$ is reduced. In other words, under the magnetic field, the present spin-charge coupled system is mapped onto a spin-less model described by $\mathscr{H}_V$ where the charge entropy plays a dominant role. On the contrary, the positive magnetic-field effect in the antiferromagnetic $CO_{1/4}$ phase is explained from the Zeeman energy. Under the magnetic field, the ferrimagnetic structure in the polar $CO_{1/3}$ phase is more stable than the antiferromagnetic one in $CO_{1/4}$, and the polarization appears below $T_{CO}(\mathbf{q}_{1/4})$. However, under a high magnetic field larger than $H/V_{abNN} \sim 0.01$, the polar $CO_{1/3}$ competes

with $CO_A$ and $CO_B$, and the polarization decreases, as discussed above.

We are also able to demonstrate the response to the electric field in the present spin-charge coupled system. The static electric field $E$ applied along the $c$ axis is formulated by the Hamiltonian

$$\mathscr{H}_E = -eEd \sum_i^u Q_i^z, \qquad (25)$$

where $d$ is a distance between the two triangular-lattice planes in a W-layer. Amplitude of the electric field $eEd/V_{abNN} = 0.01$ corresponds to about 50MV/m, when we take $V_{abNN} = 1$eV and $d = 2.2$Å. Electric-field dependence of the spin correlation functions at $V_{cNNN}/V_{abNN}=0.6$ and $0.58$ are presented in Fig. 17. By applying the electric field, the spin correlation at $\mathbf{q}_{1/3}$ is enhanced, in particular, below $T_{CO}(\mathbf{q}_{1/4})$ in $V_{cNNN}/V_{abNN}=0.58$. This is a consequence of the polar $CO_{1/3}$ phase stabilized by the electric field. The results would be use as a test for the present scenario.

## V. EFFECT OF OXYGEN DEFICIENCY

It is well known that several dielectric and magnetic properties in $R$Fe$_2$O$_4$, e.g. charge and spin ordering temperatures, are extremely sensitive to the oxygen stoicheometry, denoted by $\delta$ in the formula $R$Fe$_2$O$_{4-\delta}$.[30,32,44] Effects of the oxygen deficiency in this system are recognized as the impurity effects in charge-spin coupled system with geometrical frustration. Here we examine roles of oxygen deficiency on the magneto-electric phenomena. We simulate following two aspects of the oxygen deficiencies; 1) charge imbalance between Fe$^{2+}$ and
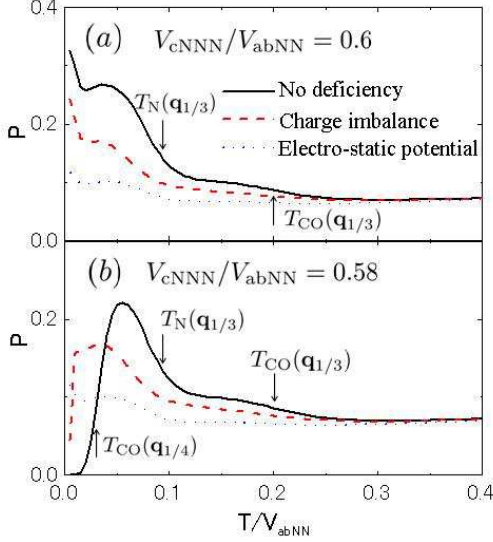
FIG. 18: Oxygen-deficiency effects of electric polarization $P$ at $V_{cNNN}/V_{abNN} = 0.6$ (a), and 0.58 (b). Bold, broken and dotted lines are for result without deficiency, that with charge-imbalance effect, and that with electro-static potential, respectively.

$Fe^{3+}$, which is introduced by the modified charge conservation relation as $N^{-1}\sum_i Q_i^z = -2\delta$, and 2) random electro-static potential around defect sites. This is modeled by the Hamiltonian

$$\mathscr{H}_R = 2\sum_i \sum_j' V_R(|i-j|)Q_j^z, \qquad (26)$$

where $\sum_i$ and $\sum_j'$ represent summations of defect sites and that of the neighboring Fe sites, respectively. We assume that a defect site is in the FeO plane, and effective charge of a defect is 2+. Amplitudes of the electro-static potentials are estimated by the $1/r$-type potential as $V_R = 1.73V_{abNN}$ and $1.60V_{abNN}$ for the NN and NNN sites from a defect site, respectively. The model Hamiltonian $\mathscr{H}_V + \mathscr{H}_J + \mathscr{H}_R$ is analyzed with the relation $N^{-1}\sum_i Q_i^z = -2\delta$ by the MUMC method. One defect is introduced in a $6 \times 6 \times 2$ site cluster. This concentration corresponds to $\delta = 0.05$.

In Fig.18, oxygen-deficiency effect on the electric polarization is presented. In $CO_{1/3}$ [see below $T_{CO}(q_{1/3})$ in Fig. 18(a) and between $T_{CO}(\mathbf{q}_{1/3})$ and $T_{CO}(\mathbf{q}_{1/4})$ in Fig. 18(b)], both the charge-imbalance and electro-static potential effects suppress the electric polarization. On the contrary, in the antiferromagnetic $CO_{1/4}$ phase below $T_N(\mathbf{q}_{1/4})$ in Fig. 18(b), the electric polarization is induced by both the two-types of deficiency effects. These results are consistent with the electron-diffraction experiments in $YFe_2O_{4-\delta}$;[44] in samples with large $\delta$, the four fold-type charge order disappears, but the three fold-type indexed as $(1/3\ 1/3\ 3m+1/2)$ is robust.

We turn to explain a mechanism of the charge-imbalance effect. Reduction of $P$ in the $CO_{1/3}$ phase shown in Fig. 18(a) is a kind of an usual impurity effect which tends to break the long-range order. On the contrary, increase of $P$ in low temperatures shown in Fig. 18(b) is related to the characteristic

charge frustration in $CO_{1/3}$ as follows. The charge imbalance represented by a relation $N^{-1}\sum_i Q_i^z = -2\delta$ implies replacement of some $Fe^{3+}$ ions in a stoichiometric system by $Fe^{2+}$. This corresponds to flipping of pseudo-spins $Q_i^z$. It is rather trivial, in Fig. 5, that this flipping of a $Q_i^z$ happens uniquely in the $CO_{1/2}$-I, $CO_{1/2}$-II and $CO_{1/4}$ structures. However, in $CO_{1/3}$, there are two ways to flip a $Q_i^z$ because of the two-sublattice structure mentioned in Sect. III: $Fe^{2+}$ sites surrounded by NN three $Fe^{2+}$ and three $Fe^{3+}$ in a plane (sublattice A), and those surrounded by six NN $Fe^{3+}$ in a plane (sublattice B). A pseudo-spin in the sublattice A is able to be flipped easily in energy. We numerically calculate energy costs due to a flipping in sublattice A is about 40% of that in sublattice B, and is about 65% in $CO_{1/2}$-II and $CO_{1/4}$. Such low-energy charge excitations in $CO_{1/3}$ stabilize the charge structure under the charge imbalance.

The electro-static potential effect is also understood from a viewpoint of a soft charge structure in the $CO_{1/3}$ phase. Since an effective charge of a defect is 2+, $Fe^{2+}$ ions, rather than $Fe^{3+}$, tend to assemble to screen this positive excess charge. However, due to the Coulombic interaction between $Fe^{2+}$ ions, a simple cluster consisting of $Fe^{2+}$ around a defect is not energetically favored. Exchange of $Fe^{2+}$ and $Fe^{3+}$ between the planes in a W-layer is able to reduce such Coulombic energy. Energy cost for this kind of exchange of $Fe^{2+}$ and $Fe^{3+}$ is much lower in $CO_{1/3}$ than that in other charge ordered structures. That is, the electro-static screening for excesses charge easily occurs in $CO_{1/3}$ because of the two-sublattice structure.

## VI. DISCUSSION AND CONCLUDING REMARK

Here we have remarks on some issues which are not included explicitly in the present model and calculation. Effects of the electron transfer in $3d$ orbitals are not taken into account in the Hamiltonian Eq. (18). This may be reasonable for the first-step theoretical model in $RFe_2O_4$. It is because, even above the three-dimensional charge-ordering temperature (250K) in $YFe_2O_4$, the electric resistivity $\rho$ shows an insulating behavior; $\rho$ increases with decreasing temperature. A magnitude of $\rho$ about 250K is of the order of $10^2 \Omega cm$,[45] which is much larger that that above the Verwey transition in $Fe_3O_4$.[46] Therefore, we suppose that dominant electron motion is caused by thermal motion, rather than quantum electron transfer. This is supported by the experimental data in the dielectric constant; it shows strong dispersive feature well described by the Debye model based on the thermal fluctuation of dipole moments.[20,27,47] Electron-transfer effects for the charge ordered phase in a triangular lattice have been investigated for some low-dimensional organic salts.[48,49] In theoretical calculations based on the $V-t$ and extended Hubbard models at quarter filling, a metallic phase appears in a parameter region between two different charge orders, or it coexists with the three-fold type charge order. We suppose that small electron transfer in $RFe_2O_4$ stabilizes the $CO_{1/3}$ phase, although diffusive features in the dielectric function becomes

more remarkable.

Lattice degree of freedom and a coupling with electron are not included explicitly in the present calculation. In our knowledge, there are no detailed crystal structure data in spin-charge ordered phases. It is thought from the experimental analyses in $YFe_2O_4$ that the crystal symmetries in both the two- and three-dimensional charge-ordered phases indexed as $(1/3\ 1/3\ 3m+1/2)$ are trigonal, but that in the four-fold type charge order is monoclinic.[44] This result indicates that the lattice distortion in the three-fold type charge order is weaker than that in other phases. This is consistent with the present results for a soft charge-order character in $CO_{1/3}$; amplitude of the charge correlation function is smaller than that in other phases. A weak lattice distortion expected in the three-fold charge order is also related to the symmetry of the $CO_{1/3}$ structure, where the rhombohedral symmetry remains in a FeO planes, unlike other charge ordered phases.

In Sect. IV, We show that the electric polarization is reinforced by the ferrimagnetic ordering, and this originates from the spin entropy due to the frustrated geometry. The long-range exchange interactions and/or the magneto-striction effects, which are not included explicitly in the present model, may release the spin degeneracy. In these cases, we suppose that the spins, which are not fixed in the present model [see Fig. 13], are loosely bounded by such low-energy scale interactions. However, these still fluctuate in a temperature region which is higher than the energy scale of the interactions, and contribute to the entropy gain.

In the present paper, we analyze an electronic model defined in a single W-layer which is recognized as a minimal and main stage in $RFe_2O_4$. Obtained results provide a starting point to elucidate a variety of magnetic and dielectric phenomena. We briefly discussed, in Sect. III, some roles of the inter W-layer Coulomb interaction. To clarify the three-dimensional charge and spin structures,[17,25,26,30] and the magneto-dielectric response along the $c$ axis, a more realistic modeling for the inter W-layer interactions, in particular, the inter W-layer exchange interactions, and analyses of a three-dimensional model are necessary.

In summary, electronic structure and magneto-dielectric phenomena in the rare-earth iron oxides with frustrated geometry are examined. The model Hamiltonian describing the electronic interactions between charge, spin and orbital degrees of freedom of Fe ions is derived. This model is analyzed by utilizing mainly the Monte-Carlo technique in a finite size cluster. The three fold-type charge order associated with electric polarization is stabilized in finite temperature in comparison with two and four fold-type charge structures. The two-sublattice structure in this polar charge order plays a crucial role. This phase is reinforced by the magnetic ordering, due to the spin frustration and the coupling between charge and spin in the exchange Hamiltonian. Novel magneto-electric responses to the external fields are available as a test of the present scenario. Effects of the oxygen deficiency are understood from the viewpoint of impurity effects in a frustrated spin-charge coupled system. Through the present study, we provide a unified scenario for a variety of magnetic and dielectric phenomena in $RFe_2O_4$.
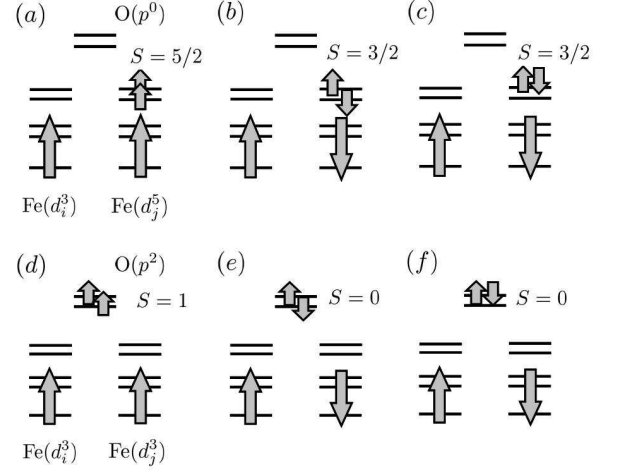


FIG. 19: Intermediate states of the exchange processes in a $Fe^{2+}$-$Fe^{2+}$ bond represented by hole picture. (a), (b) and (c) are for the Hamiltonian $\mathscr{H}^{(22)-1}$, $\mathscr{H}^{(22)-2}$, and $\mathscr{H}^{(22)-3}$ in the $dd$-processes, respectively, and (d), (e), and (f) are for $\mathscr{H}^{(22)-4}$, $\mathscr{H}^{(22)-5}$, and $\mathscr{H}^{(22)-6}$ in the $dpd$-ones, respectively. Long and short arrows represent spins with $S = 3/2$ and $1/2$, respectively.

### APPENDIX A: EXCHANGE HAMILTONIAN

In this appendix, we show details of the superexchange processes and an explicit form of the Hamiltonian $\mathscr{H}_J$ introduced in Sect. II. There are two kinds of the superexchange processes termed the $dd$- and $dpd$-processes as introduced in Eqs. (10) and (11). The Hamiltonian $\mathscr{H}_J$ is classified by valences of Fe ions, $Fe^{m+}$-$Fe^{n+}$ in the initial and final states, and the electronic structure in the intermediate states $k$ [see Eq. (13)]. In this appendix, nearest neighboring Fe sites concerning in the superexchange interactions are denoted as $i$ and $j$. Electron configuration in Fe and O ions are represented in a hole picture.

#### 1. Exchange Interactions in $Fe^{2+}$-$Fe^{2+}$

For the $dd$-processes, electron configurations in the intermediate exchange processes are denoted as $d^3p^0d^5$. Five holes are at a site $j$ and three holes at $i$ with $S = 3/2$. The intermediate states are classified by the spin and orbital states at site $j$ [see Fig. 19(a)-(c)]: (a) the total spin of Fe holes at site $j$, $S$, is equal to $5/2$ and both the two $E'$ orbitals are occupied, (b) $S = 3/2$ and the two $E'$ are occupied, and (c) $S = 3/2$ and one of the $E'$ is occupied. The explicit forms of the exchange Hamiltonian are given by

$$\mathscr{H}^{(22)-1} = J^{(22)-1} \sum_{\langle ij \rangle} (\mathbf{I}_i \cdot \mathbf{I}_j + 6)$$
$$\times \left( P_i^{\tau+} P_j^{\tau-} + P_i^{\tau-} P_j^{\tau+} \right) P_i^{Q-} P_j^{Q-}, \quad \text{(A1)}$$

$$\mathscr{H}^{(22)-2} = J^{(22)-2} \sum_{\langle ij \rangle} (\mathbf{I}_i \cdot \mathbf{I}_j - 4)$$

$$\times \left( P_i^{\tau+} P_j^{\tau-} + P_i^{\tau-} P_j^{\tau+} \right) P_i^{Q-} P_j^{Q-}, \quad \text{(A2)}$$

$$\mathscr{H}^{(22)-3} = J^{(22)-3} \sum_{\langle ij \rangle} (\mathbf{I}_i \cdot \mathbf{I}_j - 4) P_i^{\tau+} P_j^{\tau+} P_i^{Q-} P_j^{Q-}, \quad \text{(A3)}$$

Here we define the projection operators for charge

$$P_i^{Q\pm} = \frac{1}{2} \pm Q_i^z, \quad \text{(A4)}$$

and those for orbital

$$P_i^{\tau\pm} = \frac{1}{2} \pm \tau_{i\eta_i}. \quad \text{(A5)}$$

The exchange parameters are given as $J^{(22)-1} = -t_{ddc}^2/[10\Delta_{(22)-1}]$, $J^{(22)-2} = t_{ddc}^2/[10\Delta_{(22)-2}]$, and $J^{(22)-3} = t_{ddc}^2/[4\Delta_{(22)-3}]$, and $\Delta_{(mn)-k}$ is the energy of the second order intermediate states given by $\Delta_{(22)-1} = W^d - I^d + \widehat{V}$, $\Delta_{(22)-2} = W^d + 4I^d + \widehat{V}$, and $\Delta_{(22)-3} = U^d + 4I^d + \widehat{V}$. We define $t_{ddc} = t_{dd}^2 \cos\theta/\Delta_{\mathrm{CT}}$ and $t_{dds} = t_{dd}^2 \sin\theta/\Delta_{\mathrm{CT}}$.

In the intermediate states of the $dpd$-process, two holes occupy the O ion. These states are classified by the spin and orbital states at the O site, [see Fig. 19(d)-(f)]: (d) the total spin of the O holes, $S$, is equal to 1 and both the $p_x$ and $p_y$ orbitals are occupied by holes, (e) $S = 0$ and two $p$ orbitals are occupied, and (f) $S = 0$ and one of the $p$ orbitals occupied by holes. The exchange Hamiltonians are given by

$$\mathscr{H}^{(22)-4} = J^{(22)-4} \sum_{\langle ij \rangle} (\mathbf{I}_i \cdot \mathbf{I}_j + 12) P_i^{\tau+} P_j^{\tau+} P_i^{Q-} P_j^{Q-}, \quad \text{(A6)}$$

$$\mathscr{H}^{(22)-5} = J^{(22)-5} \sum_{\langle ij \rangle} (\mathbf{I}_i \cdot \mathbf{I}_j - 4) P_i^{\tau+} P_j^{\tau+} P_i^{Q-} P_j^{Q-}, \quad \text{(A7)}$$

$$\mathscr{H}^{(22)-6} = J^{(22)-6} \sum_{\langle ij \rangle} (\mathbf{I}_i \cdot \mathbf{I}_j - 4) P_i^{\tau+} P_j^{\tau+} P_i^{Q-} P_j^{Q-}. \quad \text{(A8)}$$

The exchange parameters are given as $J^{(22)-4} = -t_{dds}^2/[4\Delta_{(22)-4}]$, $J^{(22)-5} = t_{dds}^2/[4\Delta_{(22)-5}]$, and $J^{(22)-6} = t_{ddc}^2/[2\Delta_{(22)-6}]$ with $\Delta_{(22)-4} = 2\Delta_{\mathrm{CT}} + W^p - I^p$, $\Delta_{(22)-5} = 2\Delta_{\mathrm{CT}} + W^p + I^p$, and $\Delta_{(22)-6} = 2\Delta_{\mathrm{CT}} + U^p$.

### 2. Exchange Interactions in $\mathrm{Fe}^{2+}$-$\mathrm{Fe}^{3+}$

Electron configurations in the intermediate states are $d^4 p^0 d^5$ and $d^4 p^2 d^3$ for the $dd$- and $dpd$-processes, respectively. As well as the exchange interaction in the $\mathrm{Fe}^{2+}$-$\mathrm{Fe}^{2+}$ bond, these are classified by the spin and orbital structures in the $d^5$ and $p^2$ sites for the $dd$- and $dpd$-processes, respectively (see Fig. 20). The explicit forms of the exchange Hamiltonians are

$$\mathscr{H}^{(32)-1} = J^{(32)-1} \sum_{\langle ij \rangle} \left( \mathbf{J}_i \cdot \mathbf{I}_j + \frac{15}{2} \right) P_j^{\tau-} P_i^{Q+} P_j^{Q-}, \quad \text{(A9)}$$
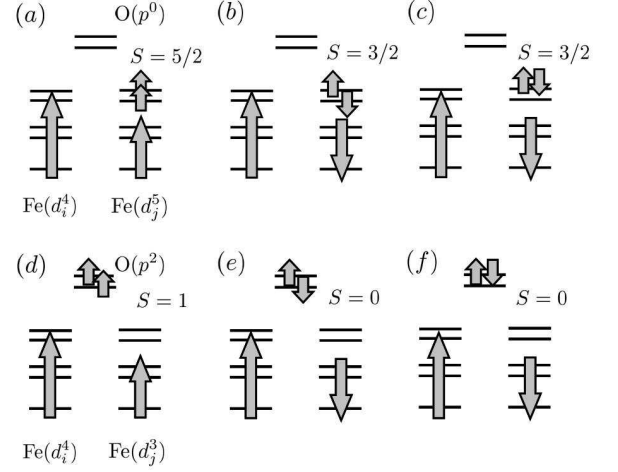


FIG. 20: Intermediate states of the exchange processes in a $\mathrm{Fe}^{2+}$-$\mathrm{Fe}^{3+}$ bond represented by hole picture. (a), (b) and (c) are for the Hamiltonian $\mathscr{H}^{(23)-1}$, $\mathscr{H}^{(23)-2}$, and $\mathscr{H}^{(23)-3}$ in the $dd$-processes, respectively, and (d), (e), and (f) are for $\mathscr{H}^{(23)-4}$, $\mathscr{H}^{(23)-5}$, and $\mathscr{H}^{(23)-6}$ in the $dpd$-ones, respectively. Long, medium and short arrows represent spins with $S = 2$, $3/2$ and $1/2$, respectively.

$$\mathscr{H}^{(32)-2} = J^{(32)-2} \sum_{\langle ij \rangle} (\mathbf{J}_i \cdot \mathbf{I}_j - 5) P_j^{\tau-} P_i^{Q+} P_j^{Q-}, \quad \text{(A10)}$$

$$\mathscr{H}^{(32)-3} = J^{(32)-3} \sum_{\langle ij \rangle} (\mathbf{J}_i \cdot \mathbf{I}_j - 5) P_j^{\tau+} P_i^{Q+} P_j^{Q-}, \quad \text{(A11)}$$

for the $dd$-processes, and

$$\mathscr{H}^{(32)-4} = J^{(32)-4} \sum_{\langle ij \rangle} (\mathbf{J}_i \cdot \mathbf{I}_j + 15) P_j^{\tau+} P_i^{Q+} P_j^{Q-}, \quad \text{(A12)}$$

$$\mathscr{H}^{(32)-5} = J^{(32)-5} \sum_{\langle ij \rangle} (\mathbf{J}_i \cdot \mathbf{I}_j - 5) P_j^{\tau+} P_i^{Q+} P_j^{Q-}, \quad \text{(A13)}$$

$$\mathscr{H}^{(32)-6} = J^{(32)-6} \sum_{\langle ij \rangle} (\mathbf{J}_i \cdot \mathbf{I}_j - 5) P_j^{\tau+} P_i^{Q+} P_j^{Q-}, \quad \text{(A14)}$$

for the $dpd$-ones. The exchange parameters are given as $J^{(32)-1} = -2t_{ddc}^2/[25\Delta_{(32)-1}]$, $J^{(32)-2} = 2t_{ddc}^2/[25\Delta_{(32)-2}]$, $J^{(32)-3} = t_{ddc}^2/[10\Delta_{(32)-3}]$, $J^{(32)-4} = -t_{dds}^2/[5\Delta_{(32)-4}]$, $J^{(32)-5} = t_{dds}^2/[5\Delta_{(32)-5}]$, and $J^{(32)-6} = 2t_{ddc}^2/[5\Delta_{(32)-6}]$ with $\Delta_{(32)-1} = \widehat{V}$, $\Delta_{(32)-2} = 5I^d + \widehat{V}$, $\Delta_{(32)-3} = U^d - W^d + 4I^d + \widehat{V}$, $\Delta_{(32)-4} = 2\Delta_{\mathrm{CT}} + W^p - I^p$, $\Delta_{(32)-5} = 2\Delta_{\mathrm{CT}} + W^p + I^p$, and $\Delta_{(32)-6} = 2\Delta_{\mathrm{CT}} + U^p$.

### 3. Exchange Interactions in $\mathrm{Fe}^{3+}$-$\mathrm{Fe}^{3+}$

Electron configurations in the intermediate states are $d^4 p^0 d^6$ and $d^4 p^2 d^4$ for the $dd$- and $dpd$-processes, respectively. In the $d^6$ configuration for the $dd$-process, total spin is
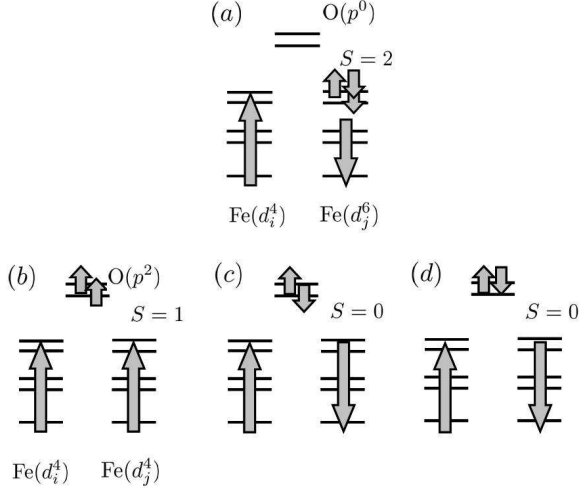
FIG. 21: Intermediate states of the exchange processes in a $Fe^{3+}$-$Fe^{3+}$ bond represented by hole picture. (a) is for the Hamiltonian $\mathscr{H}^{(33)-1}$ in the $dd$-processes, respectively, and (b), (c), and (d) are for $\mathscr{H}^{(33)-2}$, $\mathscr{H}^{(33)-3}$, and $\mathscr{H}^{(33)-4}$ in the $dpd$-ones, respectively. Long, medium and short arrows represent spins with $S = 2$, $3/2$ and $1/2$, respectively.

2 [see Fig. 21(a)], and the explicit form is given by

$$\mathscr{H}^{(33)-1} = J^{(33)-1} \sum_{\langle ij \rangle} \left( \mathbf{J}_i \cdot \mathbf{J}_j - \frac{25}{4} \right) P_i^{Q+} P_j^{Q+}. \quad \text{(A15)}$$

The exchange parameter is $J^{(33)-1} = 4t_{ddc}^2 / [25\Delta_{(33)-1}]$ with $\Delta_{(33)-1} = U^d + 4I^d + \widehat{V}$. For the $dpd$-processes, the intermediate states are classified by the spin and orbital structures in the O site [see Fig. 21(b)-(d)]. The Hamiltonians are given by

$$\mathscr{H}^{(33)-2} = J^{(33)-2} \sum_{\langle ij \rangle} \left( \mathbf{J}_i \cdot \mathbf{J}_j + \frac{75}{4} \right) P_i^{Q+} P_j^{Q+}, \quad \text{(A16)}$$

$$\mathscr{H}^{(33)-3} = J^{(33)-3} \sum_{\langle ij \rangle} \left( \mathbf{J}_i \cdot \mathbf{J}_j - \frac{25}{4} \right) P_i^{Q+} P_j^{Q+}, \quad \text{(A17)}$$

$$\mathscr{H}^{(33)-4} = J^{(33)-4} \sum_{\langle ij \rangle} \left( \mathbf{J}_i \cdot \mathbf{J}_j - \frac{25}{4} \right) P_i^{Q+} P_j^{Q+}. \quad \text{(A18)}$$

The exchange parameters are $J^{(33)-2} = -4t_{dds}^2/[25\Delta_{(33)-2}]$, $J^{(33)-3} = 4t_{dds}^2/[25\Delta_{(33)-3}]$ and $J^{(33)-4} = 8t_{ddc}^2/[25\Delta_{(33)-4}]$ with $\Delta_{(33)-2} = 2\Delta_{CT} + W^p - I^p$, $\Delta_{(33)-3} = 2\Delta_{CT} + W^p + I^p$, and $\Delta_{(33)-4} = 2\Delta_{CT} + U^p$.

## APPENDIX B: CHARGE STRUCTURES OF CO$_A$ AND CO$_B$

In this appendix, detailed charge structures in the CO$_A$ and CO$_B$ phases, introduced in Sect. III, are presented. Charge configurations of CO$_A$ are constructed from CO$_{1/3}$. Start from
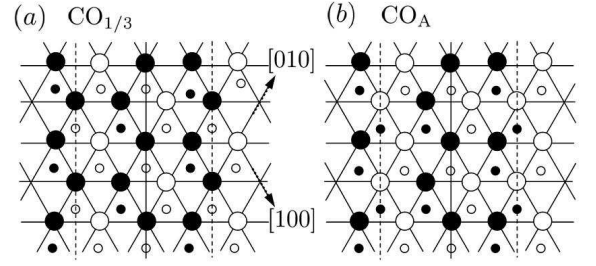


FIG. 22: Schematic pictures of the CO$_{1/3}$ structure (a) and one of CO$_A$(b). When, in CO$_{1/3}$, $Fe^{3+}$ in the upper plane and $Fe^{2+}$ in lower one on chains indicated by broken lines are exchanged, the CO$_A$ structure in (b) is obtained.
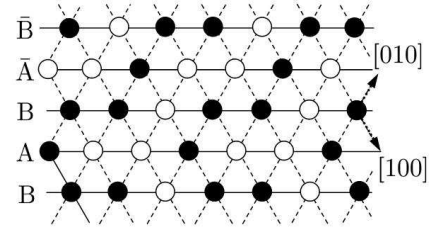


FIG. 23: One of the CO$_B$ structures.

the CO$_{1/3}$ structure shown in Fig. 22(a), and focus on chains, e.g. along $[\bar{1}10]$, where different valences of Fe ions occupy the upper and lower planes. Let exchange all $Fe^{2+}$ and $Fe^{3+}$ in any of these chains with each other. One of the obtained configurations, termed CO$_A$, is shown in Fig. 22(b). These structures of CO$_A$ are energetically degenerate with CO$_{1/3}$ in the Hamiltonian $\mathscr{H}_V + \mathscr{H}_J$. The Coulomb interaction between the 2nd NN sites in the plane may lift the degeneracy. When the number of the chains, where $Fe^{2+}$ and $Fe^{3+}$ ions are exchanged, is $n$ ($0 \le n < 2\sqrt{N}/3$), the electric polarization is $P = N/3 - n\sqrt{N}$. The degeneracy of a sum of these states is of the order of $\sum_{n} {}_{2\sqrt{N}/3}C_n \sim 2^{\sqrt{N}}$. Such exchange of Fe ions are also allowed on chains along $[120]$ and $[210]$ directions.

In another degenerated structure, CO$_B$, the configuration in one side of the W-layer is constructed by stacking two kinds of chains alternately. These chains are schematically given as $\cdots \circ \circ \bullet \circ \circ \bullet \cdots$ (termed chain $\mathscr{A}$) and $\cdots \bullet \bullet \circ \bullet \bullet \circ \cdots$ (chain $\mathscr{B}$) along the $[110]$ direction where $\bullet$ and $\circ$ represent $Fe^{3+}$ and $Fe^{2+}$, respectively. As shown in Fig. 23, without energy loss of $V_{abNN}$, there are two ways to stack a chain $\mathscr{A}$ on a chain $\mathscr{B}$, and vice versa. These are denoted as A and $\bar{A}$, and B and $\bar{B}$ in Fig. 23. Therefore, these configurations are degenerated of the order of $2^{\sqrt{N}}$. Charge configuration on another side of the W-layer is uniquely determined to gain the inter-plane Coulomb interactions $V_{cNN}$ and $V_{cNNN}$. Obtained charge structures are degenerate with the CO$_{1/3}$ structure.

**ACKNOWLEDGMENTS**

[1] T. Kimura, T. Goto, H. Shintani, K. Ishizaka, T. Arima and Y. Tokura, Nature **426**, 55 (2003).

[2] N. Hur, S. Park, P. A. Sharma, J. S. Ahn, S. Guha, and S.-W. Cheong, Nature **429**, 392 (2004).

[3] K. Saitoh, and K. Kohn, J. Phys. Condens. Matter **7**, 478 (1995).

[4] S. W. Cheong, and M. Mostvoy, Nature Mater. **6**, 13 (2007).

[5] H. Katsura, N. Nagaosa, and A. V. Balatsky, Phys. Rev. Lett **95**, 057205 (2005).

[6] M. Mostvoy, Phys. Rev. Lett **96**, 067601 (2006).

[7] I. A. Sergienko and E. Dagotto, Phys. Rev. B **73**, 094434 (2006).

[8] E. J. W. Verwey, Nature **144**, 327 (1939).

[9] See a review, for example, M. Imada, A. Fujimori, and Y. Tokura, Rev. Mod. Phys. **70**, 1039 (1998).

[10] S. Maekawa, T. Tohyama, S. E. Barnes, S. Ishihara, W. Koshibae, and G. Khaliullin, in *Physics of Transition Metal Oxides*, (Springer-Verlag, Berlin, 2004).

[11] Y. Tokura, S. Koshihara, Y. Iwasa, H. Okamoto, T. Komatsu, T. Koda, N. Iwasawa, and G. Saitoh, Phys. Rev. Lett. **63**, 2405 (1989).

[12] M. H. Lemee-Cailleau, M. Le Cointe, H. Cailleau, T. Luty, F. Moussa, J. Roos, D. Brinkmann, B. Toudic, C. Ayache, and N. Karl, Phys. Rev. Lett. **79**, 1690 (1997).

[13] K. Yamamoto, S. Iwai, S. Boyko, A. Kashiwazaki, F. Hiramatsu, C. Okabe, N. Nishi, and K. Yakushi, (preprint).

[14] Y. Tokunaga, T. Lottermoser, Y. Lee, R. Kumai, M. Uchida, T. Arima, and Y. Tokura, Nature Mater. **5**, 937 (2006).

[15] D. V. Efremov, J. van den Brink, and D. I. Khomskii, Nature Mater. **3**, 853 (2004).

[16] N. Kimizuka, E. Takayama-Muromachi, and K. Shiratori, *in Handbook on the Physics and Chemistry of Rare Earth* edited by K. A. Gshneider Jr. and L. Eyring, Vol. 13, P. 283 (Elsevier, Amsterdam, 1990).

[17] Y. Yamada, K. Kitsuda, S. Nohdo, and N. Ikeda, Phys. Rev. B **62**, 12167 (2000).

[18] Y. Yamada, S. Nohdo, and N. Ikeda, J. Phys. Soc. Jpn. **66**, 3733 (1997).

[19] Y. Zhang, H. X. Yang, C. Ma, H. F. Tian, and J. Q. Li, Phys. Rev. Lett. **98**, 247602 (2007); Y. Zhang, H. X. Yang, Y. Q. Guo, C. Ma, H. F. Tian, J. L. Luo, and J. Q. Li, Phys. Rev. B **76**, 184105 (2007).

[20] N. Ikeda, H. Ohsumi, K. Ohwada, K. Ishii, T. Inami, K.Kakurai, Y. Murakami, K. Yoshii, S. Mori, Y.Horibe, and H. Kito, Nature **436**, 1136 (2005).

[21] J. Iida, Y. Nakagawa, and N. Kimizuka, J. Phys. Soc. Jpn. **55**, 1434 (1996).

[22] J. Akimitsu, Y. Inada, K. Shiratori, I. Shindo, and N. Kimizuka, Sol. Stat. Comm. **32**, 1065 (1979).

[23] K. Shiratori, S. Funahashi, J. Iida, and M. Tanaka, Proceedings of the sixth international conference of Ferrite P. 203 (703).

[24] J. Iida, M. Tanaka, Y. Nakagawa, S. Funahashi, N. Kimizuka, and S. Takekawa, J. Phys. Soc. Jpn. **62**, 1723 (1993).

[25] A. D. Christianson, M. D. Lumsden, M. Angst, Z. Yamani, W. Tian, R. Jin, E. A. Payzant, S. E. Nagler, B. C. Sales, and D. Mandrus, arXiv:0711.3560.

[26] K. Kakurai (private communication).

[27] N. Ikeda, K. Kohn, N. Myouga, E. Takahashi, H. Kito, and S. Takekawa, J. Phys. Soc. Jpn. **69**, 1526 (2000).

[28] N. Ikeda, K. Saito, K. Kohn, Ferroelectrics **161**, 111 (1994).

[29] M. A. Subramanian, T. He, J. Chen, N. S. Rogado, T. G. Calvarese, and A. W. Sleight, Adv. Mater. **18**, 1737 (2006).

[30] S. Funahashi, J. Akimitsu, K. Shiratori, N. Kimizuka, M. Tanaka, and H. Fujishita, J. Phys. Soc. Jpn. **53**, 2688 (1984).

[31] N. Ikeda, R. Mori, K. Kohn, M. Mizumaki, and T. Akao, Ferroelectrics **272**, 309 (2002).

[32] N. Ikeda, R. Mori, S. Mori, and K. Kohn, Ferroelectrics **286**, 175 (2003).

[33] A. Nagano, and S. Ishihara, J. Phys. Cond Matt. **19**, 145263 (2007).

[34] A. Nagano, M. Naka, J. Nasu, and S. Ishihara, Phys. Rev. Lett. **99**, 217202 (2007).

[35] H. J. Xiang, and M. -H. Whangbo, Phys. Rev. Lett. **98**, 246403 (2007).

[36] J. Nasu, A. Nagano M. Naka, and S. Ishihara, (in preparation).

[37] B. Malaman, O. Evrard, N. Tannieres, A. Courtois, andJ. Protas, Acta. Crystallogr. B **31**, 1310 (1975).

[38] K. Kato, I. Kawada, N. Kimizuka, I. Shindo, and T. Katsura, Z. Kristallogr. **143**, 278 (1976)

[39] T. Mizokawa, and A. Fujimori, Phys. Rev. B **54**, 5368 (1996).

[40] Y. Mizuno, T. Tohyama, S. Maekawa, T. Osafune, N. Motoyama, H. Eisaki, and S. Uchida, Phys. Rev. B **57**, 5326 (1998).

[41] B. A. Berg, J. Stat. Phys. **82**, 323 (1996).

[42] B. D. Metcalf, Phys. Lett. **46A**, 325 (1974).

[43] When the $Fe^{2+}$ and $Fe^{3+}$ ions are distinguished, this structure has the four sublattices. However, we use, for simplicity, the two-sublattice structure.

[44] Y. Horibe, S. Shinohara, Y. Matsuo, S. Mori, K. Yoshii, and N. Ikeda (in preparation).

[45] M. Tanaka, J. Akimitsu, Y. Inada, N. Kimizuka, I. Shindo, and K. Shiratori, Sol. Stat. Comm. **44**, 687 (1982).

[46] Y. Kakudate, N. Mori, and Y. Kino, J. Mag. Mag. Mat. **12**, 22 (1979).

[47] N. Ikeda, K. Kohn, H. Kito, J. Akimitsu, and K. Siratori, J. Phys. Soc. Jpn. **63**, 4556 (1994).

[48] J. Merino, H. Seo, and M. Ogata, Phys. Rev. B **71**, 12511 (2005).

[49] C. Hotta, and N. Furukawa, Phys. Rev. B **74**, 193107 (2006).

[*] Present address: Japan Medical Materials Co., Osaka, 532-0003 Japan.